RICE UNIVERSITY

Protease-Activated Nanoshell Therapy

by

Jennifer Garner Morton

A THESIS SUBMITTED
IN PARTIAL FULFILLMENT OF THE
REQUIREMENTS FOR THE DEGREE

Master of Science

APPROVED, THESIS COMMITTEE:

Jennifer West, Professor, Chair
Bioengineering

Rebekah Drezek, Associate Professor
Bioengineering

Jason Hafner, Associate Professor
Physics and Astronomy

HOUSTON, TEXAS
APRIL, 2009

UMI Number: 1466808

INFORMATION TO USERS

The quality of this reproduction is dependent upon the quality of the copy submitted. Broken or indistinct print, colored or poor quality illustrations and photographs, print bleed-through, substandard margins, and improper alignment can adversely affect reproduction.
In the unlikely event that the author did not send a complete manuscript and there are missing pages, these will be noted. Also, if unauthorized copyright material had to be removed, a note will indicate the deletion.

UMI®

UMI Microform 1466808
Copyright 2009 by ProQuest LLC
All rights reserved. This microform edition is protected against unauthorized copying under Title 17, United States Code.

ProQuest LLC
789 East Eisenhower Parkway
P.O. Box 1346
Ann Arbor, MI 48106-1346

ABSTRACT

Protease-Activated Nanoshell Therapy

by

Jennifer Morton

This thesis describes the development of photothermal nanoshell therapy activated by proteases. Hirsch et al. previously showed that the optical spectrum of crosslinked nanoshells within the UV-visible range reveals a broader, red-shifted, and lower peak absorbance as compared to disperse nanoshells. As described in this thesis, studies showed this decrease in absorbance corresponds with a lower temperature change upon laser irradiation of the nanoshells. Near infrared (NIR)-absorbing silica-gold nanoshells were crosslinked with a proteolytically degradable linker, resulting in a broadening, red-shifting, and decrease of the peak absorbance. After collagenase was added to the crosslinked nanoshells, the peak absorbance increased, suggesting degradation of the linker and subsequent dispersion of the nanoshells. The results described here suggest that this may be applied to protease-activation *in vivo* within the tumor in an effort to increase tumor specificity and to protect surrounding normal tissue.

ACKNOWLEDGEMENTS

First, I would like to thank Jennifer West, Rebekah Drezek, and Jason Hafner for being on my committee. Then I would like to thank all of the people who have helped me out along the way. To my past and present fellow nanoshell-ers Amanda Lowery, Andre Gobin, Emily Day, and Neha Kamat: thank you for everything you have taught me and all the help you have given. Thank you to all members of the West Lab past and present for creating such a great work environment where ideas, information, help, and support are always freely available. Finally, I would like to thank my family. To my husband David: thank you for providing a listening ear and being a pillar of strength. I love you. To Mom and Dad: thank you for instilling in me a high work ethic and encouraging me in every endeavor I have pursued. I could not have done it without your love and support. I love you.

TABLE OF CONTENTS

LIST OF FIGURES

Chapter 1: Introduction

1.1 Introduction

Cancer is responsible for one out of every four deaths in the United States. For 2007, the American Cancer Society (ACS) estimates $206.3 billion in total cancer-related costs and 1,444,920 new cases[1]. In 2006, the U.S. Center for Disease Control (CDC) released a report of cancer incidence and mortality in 2003. This publication reports prostate cancer as being the leading cancer type among men and lung cancer being the leading cause of cancer death. Breast cancer is reported as being the leading cancer type among women and the second leading cause of cancer death behind lung cancer[2].

1.2 Cancer Biology

The term "cancer" refers to a disease of unchecked cell proliferation resulting in the formation of a tumor mass[3]. Defects in the cell division regulatory systems are caused by mutations in cellular DNA, specifically up-regulation of proto-oncogenes and loss of function of tumor suppressor genes. In normal cells, proto-oncogenes encode proteins involved in the growth and differentiation of cells. Mutation results in transformation into oncogenes, which allow for uncontrolled proliferation and lack of or incorrect differentiation. Tumor suppressor genes exist to inhibit cell proliferation when necessary and the loss of function likewise results in unchecked cell proliferation[3]. The physiology of the cancer cell acquires several characteristics that ultimately lead to malignant growth. These include production of their own growth signals and signal receptors, insensitivity to anti-growth signals from surrounding cells, apoptosis evasion, limitless replicative potential, sustained angiogenesis, and tissue invasion and metastasis, which is the major cause of cancer-related death[4].

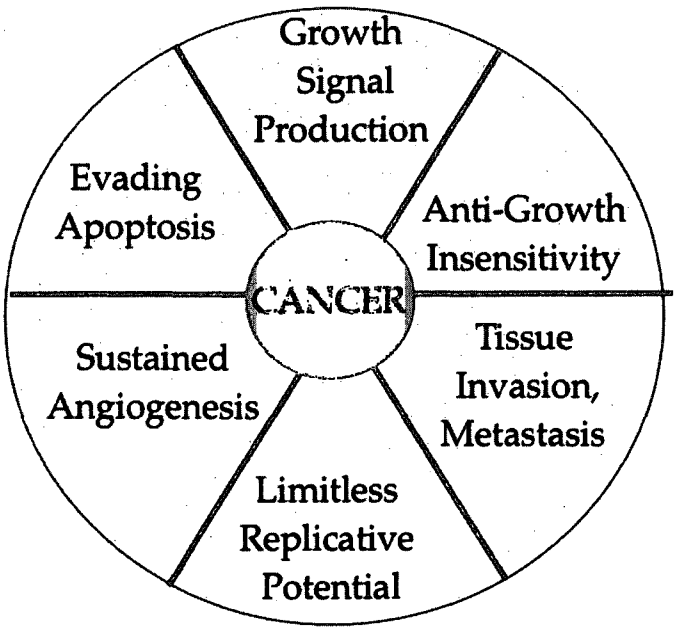

Figure 1 The hallmarks of cancer include self-sufficiency in growth signals, insensitivity to anti-growth signals, tissue invasion and metastasis, limitless replicative potential, sustained angiogenesis, and evading apoptosis. Adapted from Hanahan, 2000[4].

Due to the highly active angiogenesis and vascular remodeling, tumor vasculature is characteristically irregular (Figure 2). The vessels are disorganized, dilated, and of uneven diameter and excessive branching[5, 6], resulting in chaotic blood flow subsequently leading to hypoxic and acidic regions in the tumor[7].

The basement membrane is discontinuous or absent and the pericytes and endothelial cells are irregularly shaped. The endothelial cells do not form a

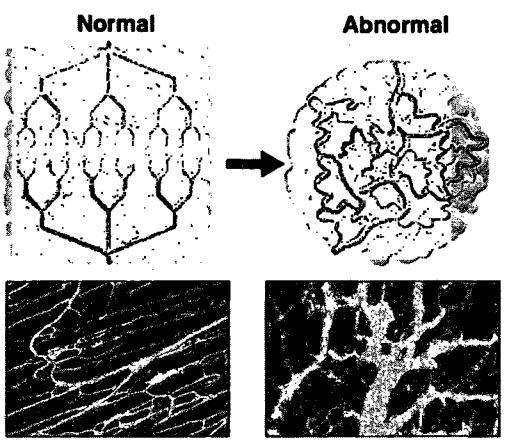

Figure 2 Tumor vasculature is irregular compared to normal tissue. The vessels of tumors are dilated, disorganized, and of uneven diameter and excessive branching. From Jain, 2005.

continuous monolayer[8, 9] due to their loose interconnections and focal intercellular openings. These openings have been shown to be up to 2 μm in diameter[10]. These characteristics lead to tumor vessels being dramatically more leaky than normal vessels[10]. By delivering nanospheres of various sizes to the tumor, Hobbs et al. demonstrated that particles from up to 780 nm in size could be delivered preferentially to subcutaneous tumors through the leaky vasculature[11].

Along with a dysfunctional vasculature, the solid tumor is also absent of functional lymphatics[12]. The lack of lymphatic clearance from the tumor interstitial space combined with the enhanced leakiness of the tumor vasculature has been characterized as the tumor-selective enhanced permeability and retention (EPR) effect[13]. This characteristic of tumors is taken advantage of in multiple tumor treatment methods.

1.3 MMPs in Tumor Metastasis

Tumor invasion and metastasis is a multi-step process in which the cancer cells detach from the tumor mass, intravasate into the blood circulation, extravasate from the circulation at a distant site, and form a secondary tumor in a new organ environment[3]. During this process, the extracellular matrix and basement membrane are digested by a family of secreted or transmembrane enzymes known as matrix metalloproteases (MMPs)[14].

Metalloproteases are a class of hydrolytic enzymes that rely on zinc for catalytic activation. The matrixin subfamily (MMPs) consists of metalloproteases that display proteolytic activity outside the cell, a conserved sequence around the cysteine residue in the propeptide, and a zinc-binding sequence, and are inhibited by tissue inhibitor of

metalloproteinase-1 (TIMP-1)[15]. The structure of MMPs, shown in Figure 3, consists of a signal sequence, followed by a propeptide domain, a catalytic domain, a hinge region, and a hemopexin domain[16]. The inactive state (proMMP) is retained by an interaction between a cysteine residue in the propeptide domain and a Zn^{+} in the catalytic domain. Dissociation of this reaction results in activation of the enzyme[15].

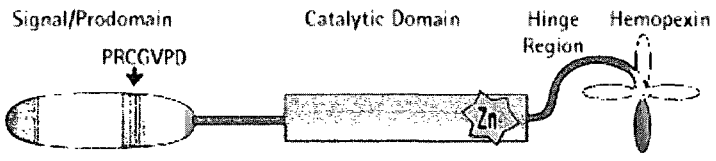

Figure 3 The structure of matrix metalloproteases (MMPs) consist of a signal sequence, propeptide domain, catalytic domain, a hinge region, and a hemopexin. From www.emdbiosciences.com[17].

MMPs can be both secreted as soluble enzymes or membrane-bound and are divided into subgroups based on substrate specificity[15]. These categories include collagenases (MMP-1, MMP-8, and MMP-13), gelatinase A (MMP-2) and gelatinase B (MMP-9), stromelysins (MMP-3, MMP-10, and MMP-11), and a metalloelastase (MMP-12), the majority of which are secreted, and membrane-type MMPs (MT-MMPs) which are membrane-bound[14]. MMPs are used to degrade the ECM in normal physiological functions including embryonic development, wound healing, and angiogenesis[15].

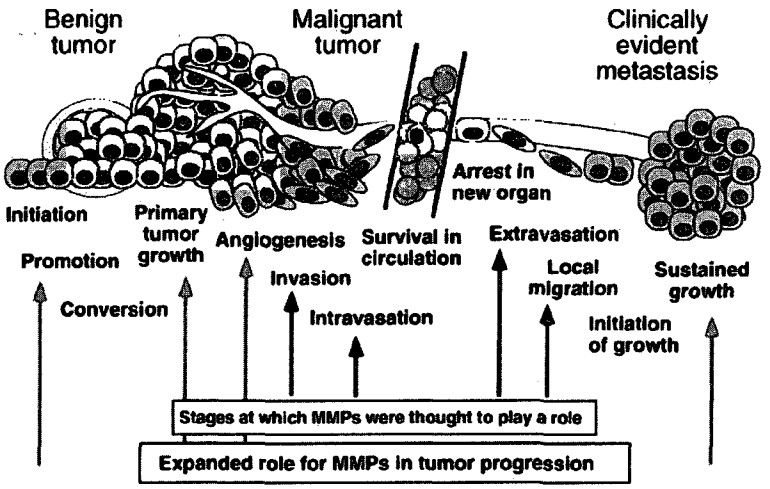

Figure 4 Roles of MMPs in tumor progression and angiogenesis[18].

Gelatinase A (MMP-2) degrades the basement membrane components type IV collagen and laminin[19] and has been identified in metastatic tumors[20, 21]. MT1-MMP, which degrades type I and II collagens, fibronectin, vitronectin, laminin, fibrin, and proteoglycan, activates proMMP-2, the inactive form of MMP-2[22]. MT1-MMP has been shown to be present in high levels in many malignant tumor tissues[23]. As a result, high levels of activated MMP-2 has been shown in many types of human cancers, including oral[24], gastric[25], lung[26], prostate[27], ovarian[28, 29], bladder[30], and breast[31]. MMP-9, also known as gelatinase B, also plays an important role in tumor initiation, growth, and metastasis[14]. Its expression has been shown to correlate with metastatic potential[32].

Unlike the majority of MMPs that are secreted predominantly by stromal cells of the tumor, matrilysin (MMP-7) is produced by the tumor cells[33]. This protease is overexpressed in cancers of the digestive system as well as that of the lung, skin, prostate,

breast, and head and neck[33]. Matrilysin degrades ECM substrates such as elastin, type IV collagen, fibronectin, and laminin[34] and activates proMMP-2 and proMMP-9[35].

1.4 Cancer Therapy

Easily accessible benign tumor masses can be removed through surgery. For malignant tumors or those that cannot be safely surgically removed, additional methods of treatment are required. Radiation therapy seeks to damage the DNA of rapidly dividing cells in order to disrupt the cell cycle and subsequently halt cell growth. The ionizing radiation can be administered from either an external or internal source[36]. External beam radiation therapy (EBRT) delivers high doses of X-rays to the tumor area, located by computed tomography (CT) scan. Three-dimensional conformal radiotherapy (3D-CRT) shapes the beams to the shape of the tumor, thereby reducing the amount of normal tissues exposed to the radiation[37]. Intraoperative radiation therapy (IORT) applies radiation during surgery in order to treat localized tumors that cannot be completely removed surgically[36, 38]. Internal radiation (brachytherapy) involves applying radiation in very close proximity to the tumor area through an implant including balloons[39], catheters, hollow needles[40], among others.

The goal of chemotherapy drugs is to damage the DNA in rapidly dividing cells in order to slow or completely halt the cell cycle. Specific chemotherapeutic drugs and their mechanism of action are summarized in Table 1.

Table 1 Commonly used chemotherapy drugs and their mechanisms of action

Drug Type	Mechanism of Action	Cancer Types	Examples
Alkylating Agents	Alkylates oxygen and nitrogen atoms in nucleotides[41]	Leukemia, Hodgkin disease, multiple myeloma, lung, breast, ovarian	Busulfan, cisplatin, carboplatin, chlorambucil, ifosfamide
Anti-metabolites	Incorporates into DNA – recognized by mismatch repair system – cell cycle arrest[42]	Leukemia, breast, ovary, GI tract, colon	5-fluorouracil, 6-mercaptopurine, methotrexate
Nitrosoureas	Crosslinks guanine and cytosine on opposite DNA strands[41]	Brain, lymphoma, multiple myeloma, malignant myeloma	Streptozocin, carmustine, lomustine
Plant Alkaloids	Inhibit mitosis	Breast, lung, myeloma, lymphoma, leukemia	Taxanes (paclitaxel, docetaxel) and vinca alkaloids (vinblastine, vincristine)
Topoisomerase Inhibitors	Inhibit enzymes that catalyze relaxation of supercoiled DNA[42]	Leukemia, lung, ovarian, GI tract	Topotecan, etoposide
Antitumor Antibiotics	Inhibits topoisomerase II; generates free radicals	Leukemia, breast, bladder, lung, ovaries	Daunorubicin, doxorubicin, mitoxantrone
Corticosteroid Hormones	Prevent phospholipids release, decrease eosinophil action; promote Na^+ retention in kidney	Lymphoma, leukemia, multiple myeloma	Prednisone, solumedrol, dexamethasone

Because chemotherapy is normally administered systematically, normal healthy cells are often damaged along with the cancer cells, resulting in many unwanted side effects such as nausea and hair loss. In order to lessen the side effects that result from systemically

administering DNA-damaging drugs, other strategies have been developed including the use of angiogenesis inhibitors[43] and photodynamic therapy[44].

1.5 Nanoparticles in Cancer Therapy and Diagnostics

The use of nanoparticles in the tumor-selective delivery of anticancer agents and as contrast agents for *in vivo* tumor imaging has been explored. Nanoparticles potentially provide the ability to shield healthy tissue from the exposure to cytotoxic anticancer drugs while en route to the tumor. Anthracycline agents, such as doxorubicin have been encapsulated in liposomes (100 nm diameter) in an effort to reduce its cytotoxic effects[45, 46]. Due to their hydrophobicity, taxanes such as paclitaxel and docetaxel must be transported to the tumor site in synthetic vesicles. These synthetic materials often exert cytotoxic effects. Cremophor EL (CrEL), the surfactant utilized in the solubilization of paclitaxel, induces acute hypersensitivity and neurotoxic effects[47]. The use of non-synthetic materials as a delivery vehicle is being explored. Albumin-encapsulated taxanes have shown both effectiveness in tumor penetration and low toxicity[48]. Dendrimers and carbon nanotubes are also currently being explored in potential drug delivery methods[49, 50].

Nanoparticles are gaining attention as potential contrast agents in various imaging methods because of the ability to functionalize the nanoparticle surface with targeting moieties. Magnetic nanoparticles encapsulated by a gold shell are being explored potential contrast agents for MRI[45, 51]. Polymer-encapsulation is an effective means of delivering contrast agents that are not effective when uncoated. Bismuth is stable at high concentrations, has an X-ray absorption five times higher than iodine, demonstrates long *in vivo* circulation times, and expresses an efficacy/safety profile comparable to that

of iodine[52]. Bismuth, however, is not effective when uncoated because of nanocrystal aggregation at physiologic pH and potential plasma protein adsorption on the surface[52]. Rabin et al. coated bismuth nanoparticles in polyvinylpyrrolidone (PVP) and demonstrated its efficacy as a contrast agent in CT imaging[52].

Quantum dots are a potential alternative to *in vivo* organic immunofluorescence. Quantum dots are semiconductor nanoparticles that are detectable *in vivo* under NIR light when made to emit in the near-infrared spectrum[45]. These quantum dots can therefore be surface-functionalized with tumor-targeting agents and utilized for *in vivo* tumor localization.

1.6 Nanoshell Therapy and Imaging

Nanoshells are optically tunable nanoparticles consisting of a dielectric core and a thin metal shell. These particles can be designed to primarily scatter or absorb light based on the core and shell dimensions. A larger core results in greater scattering contr3ibution to the total extinction while a smaller core typically induces primarily absorbing properties. The location of the peak extinction within the spectrum is dependent upon the ratio of the core radius to shell thickness, as demonstrated in Figure 5. A thinner shell induces a shift of peak extinction to the longer wavelengths, while a thicker shell produces a peak blueshift[53].

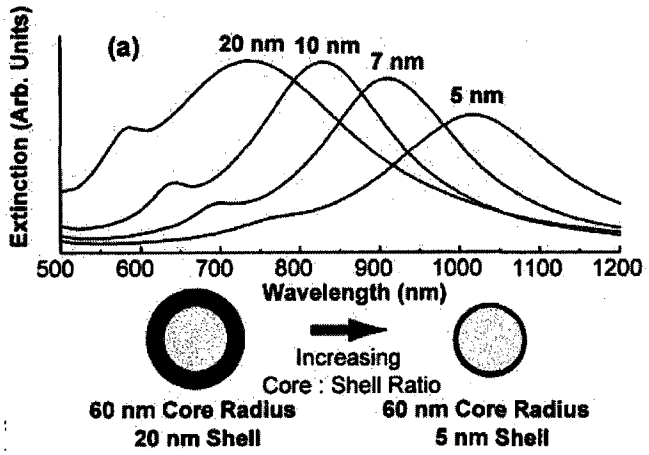

Figure 5 The optical properties of nanoshells are dependent on the core size/shell thickness ratio. With a dielectric core of the same size, a thinner gold shell results in a redshifted peak while a thicker shell pushes the peak to shorter wavelengths[53].

Due to their ability to either scatter or absorb light, nanoshells possess great potential in both imaging and therapeutic applications, specifically optical imaging and photothermal ablation of tumors. Other applications include tissue welding[54] and probes for antigen detection in whole blood[55]. This section describes in detail the development of nanoshells, their physical optical properties, and their use in tumor therapeutic and imaging applications.

1.6.1 Optical Properties of Nanoshells

Nanoparticles with a dielectric core of Au_2S and a gold shell were the first core/shell nanoparticle to be described experimentally[46, 56, 57]. These nanoparticles are formed by mixing aqueous solutions of Na_2S and $HAuCl_4$. The proposed reaction of the reduction process is

$$2AuCl_4^- + 3HS^- \leftrightarrow 2Au + 3S + 3H^+ + 8Cl^-,$$

after which Au and S are available for nucleation and growth. Under these reaction conditions, both Au particles and Au-coated Au_2S particles are grown simultaneously. A

two-stage growth model of the Au_2S particles is proposed in which a linear increase in Au shell thickness follows linear growth of the core radius. The growth of the core radius contributes to the redshift of the near infrared peak and upon reaching a constant size, the peak takes a turn towards smaller wavelengths as the shell thickness increases[46]. Figure 6 shows spectra are taken at various time points during particle growth where the presence of two peaks is observed. The largest peak, located at 530nm, is attributed to the pure gold particles present in the solution. The second peak, in the near infrared region, starts out almost non-existent then grows larger as the reaction proceeds, initially shifting toward longer wavelengths and then taking a sudden blueshift turn.

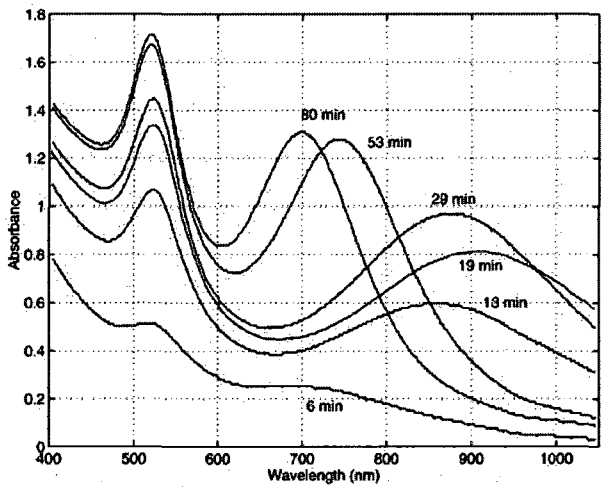

Figure 6 UV-visible spectra of gold-gold sulfide nanoshells taken at various time points during particle growth show the plasmon resonance shifts initially toward longer wavelengths and then blueshifts[46].

Nanoshells are unique nanoparticles in that their optical properties are dependent on the core diameter to shell thickness ratio. This property is described by the Mie theory, the solution for the Maxwell equations for a dilute colloidal system. Extending the Mie theory to nanoparticles with a metal shell involves specifying the boundary

conditions at one additional interface, that of the core and shell. Because $r << \lambda$ for these nanoparticles, where r is the particle radius and λ is the wavelength of the incident electromagnetic field, the quasi-static approach can be used in order to simplify Mie theory calculations. In this model, the electromagnetic incident field does not vary spatially over the diameter of the diameter of the metal shell and therefore the spatial variance is neglected in the calculations. The time-dependence of the incident wave, however, is preserved. For further simplification, the nanoshells are assumed to be perfectly spherical and interactions between nanoparticles are neglected due to the low nanoshell concentration[56].

Averitt et al. derived and described this quasi-static theory of nanoshells[56]. The geometry of the nanoshell is shown in Figure 7 where r_1 is the core radius, r_2 is the total particle radius, and ε_1, ε_2, and ε_3 are the dielectric constants of the core, shell, and medium, respectively.

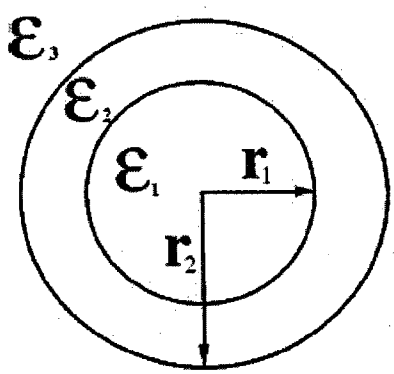

Figure 7 The geometry of a nanoshell. r_1 is the core radius while r_2 is the total particle radius. ε_1, ε_2, and ε_3 are the dielectric constants of the core, shell, and medium, respectively[56].

Applying the Mie scattering theory, the absorption cross section of the nanoshells obtained is described by Equation 2

$$\sigma_{abs} = \frac{k}{\varepsilon_0}\mathrm{Im}(a), \qquad \textbf{Equation 2}$$

where the polarizability (a), the tendency of charge distribution to be distorted by an external electric field, is described by Equation 3

$$\alpha = 4\pi\varepsilon_o r_2^3\left[\frac{\varepsilon_2\varepsilon_a - \varepsilon_3\varepsilon_b}{\varepsilon_2\varepsilon_a + 2\varepsilon_3\varepsilon_b}\right]. \qquad \textbf{Equation 3}$$

Combining Equations 2 and 3, the absorption cross section is given as

$$\sigma_{abs} = \frac{8\pi^2\sqrt{\varepsilon_3}}{\lambda} r_2^3\,\mathrm{Im}\left(\frac{\varepsilon_2\varepsilon_a - \varepsilon_3\varepsilon_b}{\varepsilon_2\varepsilon_a + 2\varepsilon_3\varepsilon_b}\right), \qquad \textbf{Equation 4}$$

where

$$\varepsilon_a = \varepsilon_1(3-2P) + 2\varepsilon_2 P, \qquad \textbf{Equation 5}$$

$$\varepsilon_b = \varepsilon_1 P + \varepsilon_2(3-P), \qquad \textbf{Equation 6}$$

and P, the shell volume to total particle volume ratio, is described by

$$P = 1 - \left(\frac{r_1}{r_2}\right)^3. \qquad \textbf{Equation 7}$$

Similarly, the scattering cross section is described as

$$\sigma_{sca} = \frac{128\pi^5}{3\lambda^4}\varepsilon_3^2 r_2^6\left|\frac{\varepsilon_2\varepsilon_a - \varepsilon_3\varepsilon_b}{\varepsilon_2\varepsilon_a + 2\varepsilon_3\varepsilon_b}\right|^2. \qquad \textbf{Equation 8}$$

Figure 8 shows the nanoshell extinction cross sections using Equations 3 and 7 where $r_2 = 4.\ 10,\ 17.$

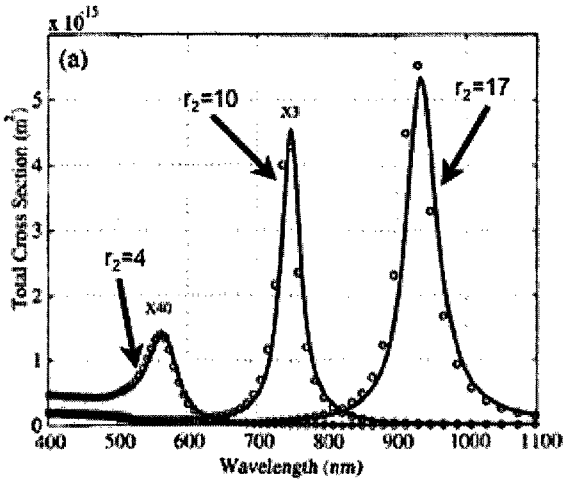

Figure 8 Calculations of the nanoshell absorption and scattering cross sections with a shell thickness of 2 and r_2 = 4, 10, 17 indicates that, for a given shell thickness, a larger core diameter yields a plasmon resonance shifted to longer wavelengths[56].

This demonstrates the dependency of the resonance wavelength on the ratio of core radius to total particle radius. For a given shell thickness, a larger particle diameter yields a peak plasmon resonance in the longer wavelengths[56].

The plasmon resonance of the electrons in the metal shell occurs at the point of maximum polarizability. From Equation, it can be seen that this is when the denominator approaches zero ($\varepsilon_2\varepsilon_a + 2\varepsilon_3\varepsilon_b \rightarrow 0$). From Equation and the previous definitions, Averitt et al developed the following expression describing the plasmon resonance as a function of wavelength if both the core and embedding medium are dielectrics:

$$\frac{r_1}{r_2} = \left[1 + \frac{3}{2}\frac{\varepsilon'(\lambda)(\varepsilon_1 + 2\varepsilon_3)}{\left[\varepsilon_2'(\lambda)\right]^2 - \varepsilon_2'(\lambda)(\varepsilon_1 + \varepsilon_3) + \left\{\varepsilon_1\varepsilon_3 - \left[\varepsilon_2''(\lambda)\right]^2\right\}}\right]^{\frac{1}{3}}, \qquad \textbf{Equation 9}$$

when $r_2 << \lambda$, shell thickness $(r_2 - r_1)$ is greater than a few atomic layers. This expression demonstrates the fact that the wavelength of plasmon resonance is dependent on the core/shell geometry of the particle[56].

Due to the tunability of the optical properties, the ability to control the core and shell dimensions is desirable. Oldenburg et al. developed a nanoshell with a dielectric silica core and a gold shell[53]. The silica cores are made using the Stöber method in which tetraethyl orthosilicate is reduced in ammonium hydroxide (NH_4OH) in ethanol. The size of the silica particles is correlated with the amount of NH_4OH added to the solution, therefore providing control over core size. The shell is formed by reducing gold colloid particles on the surface of the core. The size of the shell is dependent on the relative amount of gold to silica cores during the reduction process, thereby providing control over the shell thickness.

1.6.2 Optical Properties of Crosslinked Nanoshells

When nanoshells are cross-linked, the peak extinction red-shifts, broadens, and decreases (Figure 9).

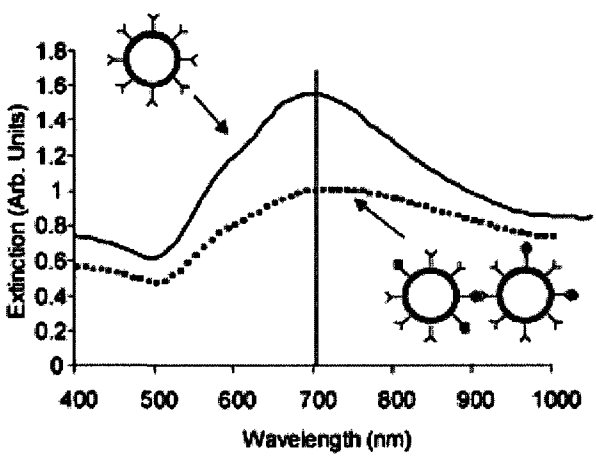

Figure 9. Crosslinked nanoshells experience a red-shifting, broadening, and decrease in peak extinction[55].

This is due to the fact that nanoshells that are linked together in very close proximity are acted upon by the dipole fields of the other particles in the aggregate as well as the

incident field. The absorption cross-section of nanoparticle aggregates is described by the equation

$$C_{abs} = \frac{4\pi k}{|\mathbf{E}_{inc}|^2} \sum_{j=1}^{N} \{Im\{\mathbf{P}_j \bullet (a_j^{-1}) * \mathbf{P}^*\} - \frac{2}{3} k^3 \mathbf{P}_j \bullet \mathbf{P}^*_j\}, \qquad \textbf{Equation 10}$$

which represents a summation of the rate of energy dissipation by each of the dipoles. The first term of the summation ($\mathbf{P}_j \bullet (a_j^{-1}) * \mathbf{P}^*$) represents the energy of the incident electromagnetic field. The second term ($(2/3)k^3\mathbf{P}_j$) represents the combined electric field experienced by j due to the other N-1 dipoles, also known as the radiative reaction.[58, 59].

1.6.3 Nanoshell-Assisted photothermal therapy

The tunability of nanoshells enables potential use in biological applications in that they can be designed to strongly absorb light in the near infrared (NIR) region (650-900 nm). In this range, the absorption coefficients of water and hemoglobin are at their lowest, and therefore light is able to penetrate deeply into tissues (Figure 10) [60].

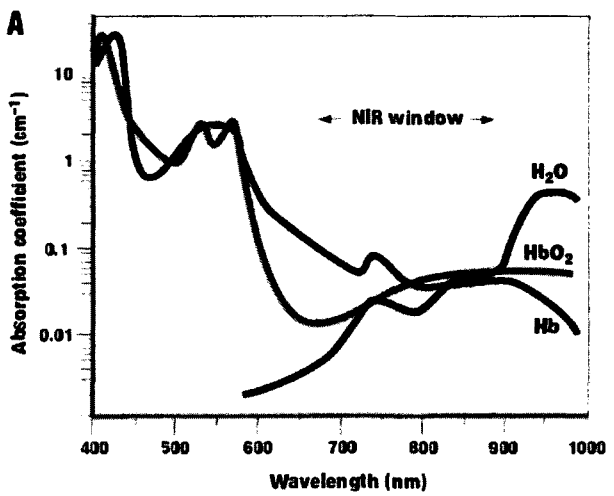

Figure 10 In the NIR window, the absorption coefficients of water and hemoglobin are at their lowest, enabling light of wavelengths within this range to deeply penetrate tissue[60]

When injected systemically, NIR-absorbing nanoshells have been shown to extravasate out of the leaky tumor vasculature where, when irradiated with a NIR laser, they generate heat, resulting in photothermal destruction of the tumor[61]. This section describes the development of this method known as nanoshell-assisted photothermal therapy (NAPT).

The first use of nanoshells in photothermal ablation of tumors was shown by Hirsch et al. in 2003[62]. SKBr3 human breast epithelial carcinoma cells were incubated *in vitro* with nanoshells and then irradiated with NIR light. Cells without nanoshells were irradiated with the laser as a control. Calcein AM staining (Figure 11) revealed a circle of cell death corresponding to the spot size of the laser in the nanoshell-treated shells and no death in the cells that were treated with the laser only. Fluorescein-dextran, a high molecular-weight dye impermeable to healthy cells, was shown to penetrate the membranes of the cells receiving the nanoshell/laser treatment. This implies that cell membrane destruction is a mechanism involved in cell death resulting from nanoshell/laser treatment.

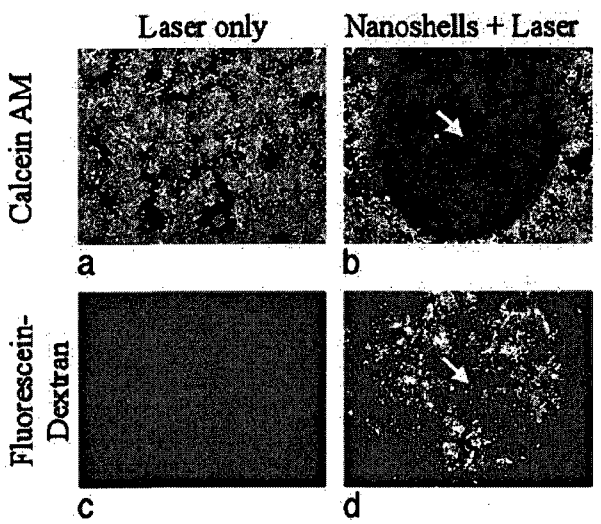

Figure 11 Calcein AM staining shows cell death in those cells receiving nanoshell treatment (a,b). High molecular weight dye indicates membrane destruction as the mechanism of cell death (c,d)[62].

In addition to the previously mentioned study, nanoshell treatment of tumors in mice and the resultant heat profiles within the tumors were investigated[62]. Mice were inoculated with canine TVT cells on both hind legs. After the tumors reached a diameter of 1 cm, nanoshells were injected interstitially into the tumor. Prior to injection, the nanoshell surfaces were functionalized with poly(ethylene glycol) thiol (PEG-SH) to provide steric stabilization and to minimize aggregation due to protein adsorption in the physiological environment. Five to thirty minutes after injection, the tumor sites were exposed to the NIR laser. Magnetic resonance thermal imaging (MRTI) was used to monitor the temperature distribution within the tumor during treatment. Nanoshell-treated tumors resulted in an average temperature increase of 37.4 ± 6.6°C, high enough to cause irreversible tissue damage, while nanoshell-free controls experienced an average temperature increase of only 9.1 ± 4.7°C. Gross pathology, silver staining, and histology of the tumors indicated edema, coagulation, cell shrinkage, and loss of nuclear staining in the same area as the localized nanoshells (Figure 12) [62].

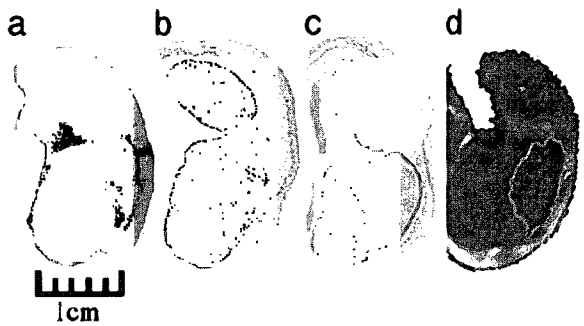

Figure 12 Analysis of an excised tumor from a mouse receiving nanoshell-assisted photothermal therapy reveals that the area of tissue damage coincides with the area of localized nanoshells. (a) gross pathology reveals hemorrhaging, (b)silver staining reveals the area of localized nanoshells, (c) hematoxylin/eosin staining reveals the area of tissue damage, and (d) MRTI calculations reveal the area of irreversible thermal damage[62].

O'Neal et al. investigated NAPT in mice with delivery to the tumor site through the vasculature[61]. Mice were inoculated subcutaneously with CT26 colon carcinoma tumor cells and when the tumor reached 3-5.5 mm diameter, PEGylated nanoshells were injected into the tail vein. To allow enough time for the nanoshells to accumulate in the tumor site, laser treatments were performed 6 hours after nanoshell injection. Within 10 days of treatment, complete resorption of the tumors was observed in the nanoshell-treatment group (Figure 13) and 90 days after treatment, all nanoshell-treated mice were healthy and tumor-free. Tumors in the control groups continued to grow rapidly and all mice were euthanized by day 19 due to excessive tumor growth.

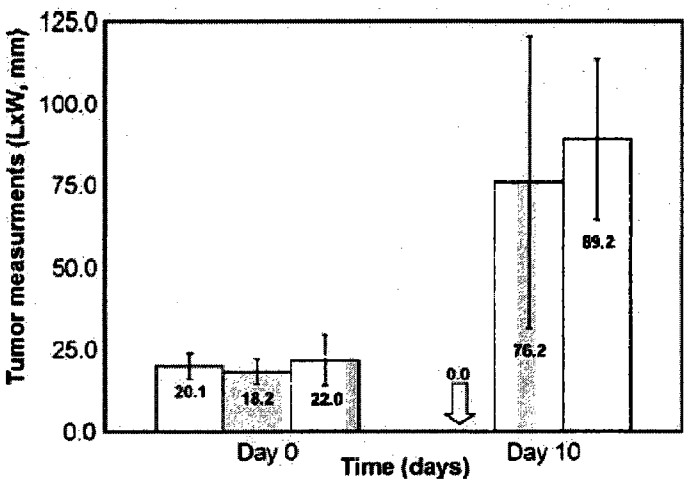

Figure 13 Meant tumor size measured on treatment day (day 0) and 10 days post-treatment. All tumors receiving NAPT showed resorption after 10 days[61].

1.6.4 Immunotargeted Nanoshells

In order to increase nanoshell specificity to the tumor site, targeting the nanoshells with antibodies against overexpressed cell-surface oncoproteins has been investigated[63]. In order to target human epidermal growth factor receptor 2 (HER2), which is over-expressed on human breast cancer cells, nanoshells were targeted using the

anti-HER2 antibody. HER2+ SKBr3 cells were incubated with antibody-functionalized nanoshells and then irradiated with a NIR laser. Nanoshells conjugated to anti-IgG, a nonspecific control antibody, served as a control. Following laser irradiation, the cells were stained with calcein AM, which indicated a circular area of cell death corresponding to the spot size of the laser for those cells incubated with targeted nanoshells. No cell death was observed for cells incubated with non-targeted nanoshells or for cells receiving only laser irradiation (Figure 14).

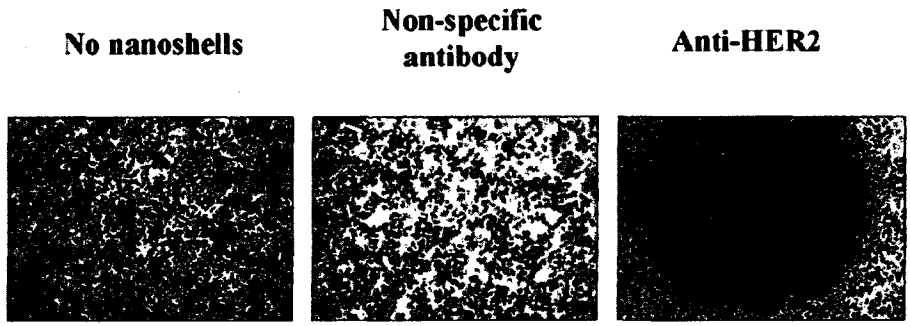

Figure 14 Therapy of SKBr3 cells using HER2-targeted nanoshells. Calcein staining reveals cell death in cells receiving NIR-laser treatment following exposure to HER2-targeted nanoshells[63].

Targeting the tumor vasculature itself has also been investigated[64]. Vascular endothelial growth factor receptor-2 (VEGFR-2), a tyrosine kinase receptor expressed on the surface of endothelial cells that is upregulated in tumor vasculature[65-67], was the target of choice. Targeting to VEGFR-2 using $VEGF_{165}$ and anti-VEGFR-2 antibodies was explored. Parallel experiments were run investigating VEGFR-2 targeting *in vitro*. In one experiment, $VEGF_{165}$ was conjugated to the nanoshells surface and in the other, anti-VEGFR-2. Murine endothelial Miles Sven 1 (MS1) cells and human dermal fibroblasts (HDFs) were incubated with VEGF or VEGFR-2 conjugated nanoshells. The cells were then irradiated with a NIR laser at 60 W/cm^2 for 7 minutes over a 1.5 mm

diameter spot. Live/dead staining revealed a circular area of cell death the same spot size as that of the laser for VEGF and anti-VEGFR-2 conjugated nanoshells on MS1 cells (Figure 15). No cell death of MS1 cells was observed as a result of non-targeted nanoshells and no cell death of the HDFs occurred.

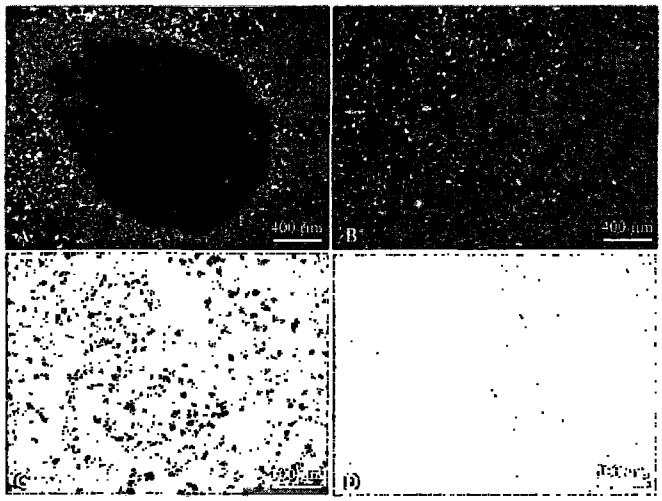

Figure 15 Cell viability and silver staining after laser + anti-VEGFR conjugated nanoshell therapy. A) Circular area of cell death as a result of laser exposure to MS1 cells incubated with anti-VEGFR nanoshells. B) No cell death resulting from non-targeted nanoshells. C) Silver staining verifies binding of anti-VEGFR nanoshells to MS1 cells. D) Very minimal binding of non-targeted nanoshells to cells[64].

In order to study VEGF nanoshell targeting *in vivo*, female BALB/c mice were inoculated subcutaneously with CT-26 cells, forming a tumor on the right hind flank[64]. Tumors were allowed to grow 6-10 days after which they were injected with nanoshells through the tail vein. Three mice received VEGF nanoshells plus laser, three received non-targeted nanoshells plus laser, and three received no treatment. The nanoshells were allowed to accumulate in the tumor for 2 hr prior to laser exposure (820 nm, 4 W/cm^2, 3 minutes). Measurements of the tumor size in the days following laser treatment revealed

a minimization of tumor burden in the mice receiving VEGF-nanoshells but not in those receiving non-targeted nanoshells or no therapy (Figure 16).

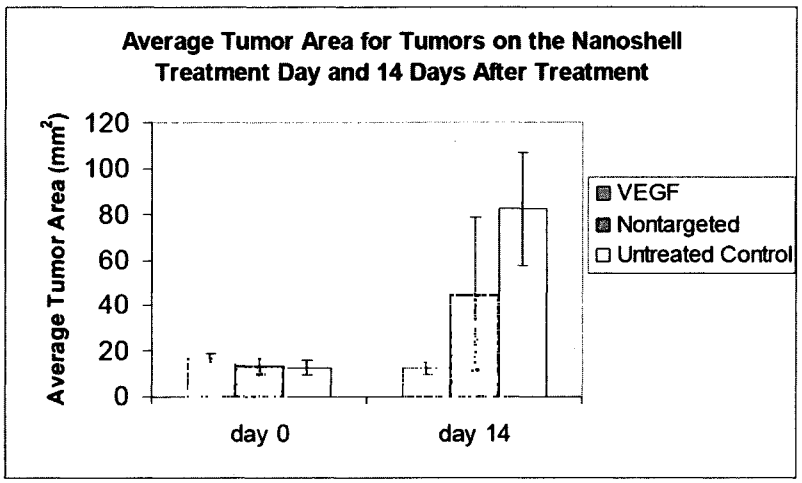

Figure 16 Average tumor area of tumors on the day of treatment and 14 days after treatment. The average tumor area for mice receiving VEGF-nanoshells was comparable to the tumor size on the day of the treatment. The tumors of mice receiving either non-targeted nanoshells or no treatment continued to grow[64].

1.6.5 Nanoshell-Assisted imaging techniques

As mentioned previously, nanoshells can be designed to strongly scatter light, which is of great use in optical imaging modalities. Their use in *in vitro* dark-field imaging of HER2 expression using has been described[63, 68, 69]. Nanoshells with a 120 nm core radius and a 35 nm shell thickness were conjugated to anti-HER2 and incubated with HER2+ SKBr3 cells and then imaged under dark-field magnification[69]. Figure 17 demonstrates the contrast provided by targeted nanoshells as opposed to non-targeted or the absence of nanoshells.

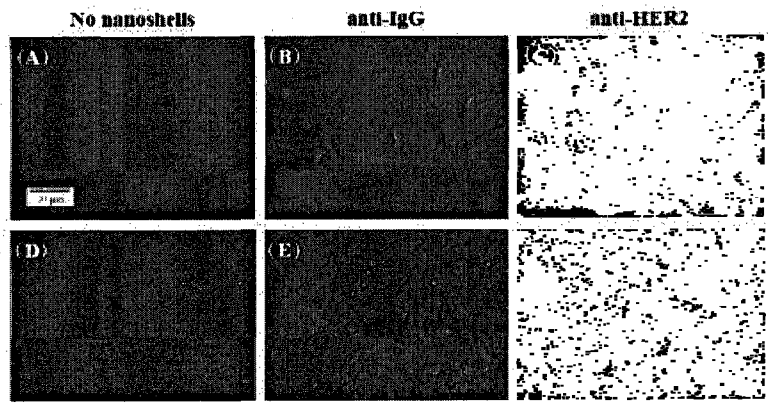

Figure 17 Scattering properties of nanoshells. (a-c) High magnification (40X) dark field images of HER2+ SkBr3 cells incubated with no nanoshells, angi-IgG-labeled nanoshells, and HER-2 targeted nanoshells. (d-f) Dark-field images (10X) of HER2+ cells[69].

Nanoshells have also been investigated in the use of signal enhancement in optical coherence tomography (OCT). Loo et al. compared OCT images of saline, a suspension of 2 μm polystyrene microspheres, and a nanoshell (100-nm core radius, 20-nm shell thickness) suspension at a concentration of $1x10^9$ NS/ml. Basing OCT intensity on a log scale where black=255 and white=0, the average intensity of saline was 247 while nanoshell intensity was 160, showing that nanoshells provided higher contrast[68].

Due to their ability to be designed to both scatter and absorb light, nanoshells can be used in combined imaging and therapy applications. This was first demonstrated with an *in vitro* study in which SKBr3 cells were incubated with HER2-targeted nanoshells followed by laser irradiation (820 nm, 0.008 W/m^2, 7 min)[63]. Cell viability was then assessed via calcein staining and nanoshell binding was assessed through silver staining. The nanoshells bound to cells were viewed using darkfield microscopy. Figure 18 shows increased contrast and cytotoxicity in cells resulting from targeted nanoshell/laser therapy compared to both cells treated with non-targeted nanoshells and laser irradiation and cells treated with laser only.

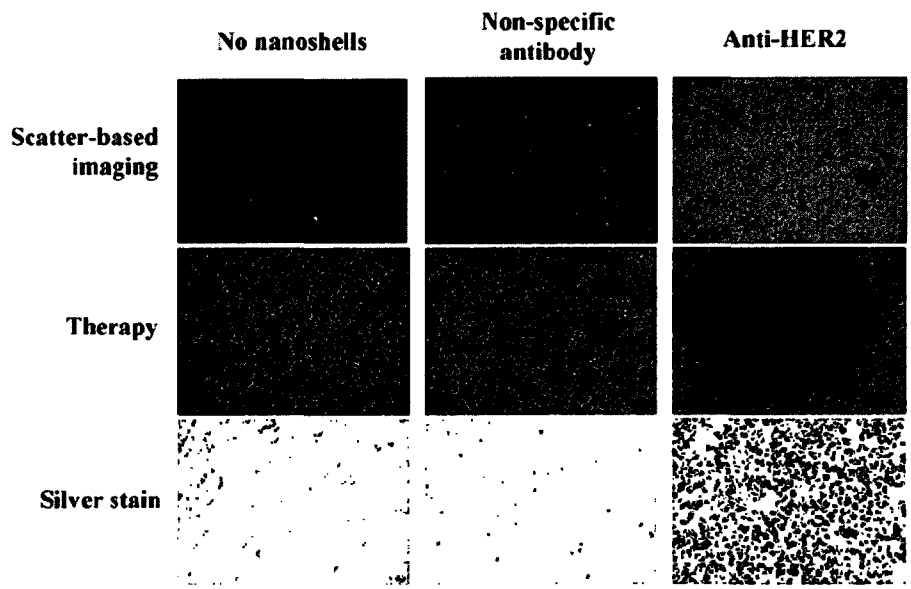

Figure 18 Combined imaging and therapy of SKBr3 cells using HER2-targeted nanoshells. (Top row) Dark-field imaging. (Middle row) Calcein staining revealing cell death in nanoshell-treated cells. (Bottom row) Silver stain imaging of targeted nanoshells[63].

Gobin et al. investigated the application of nanoshells in combined imaging and therapy *in vivo*[70]. Nanoshells were made with a core diameter of 119 nm and a shell thickness of 12 nm. Mice were subcutaneously inoculated with CT-26 cells on the right hind flank, forming a tumor. Tumors were allowed to grow to a diameter of 5 mm after which PEG-conjugated nanoshells were injected into the mice through the tail vein. PBS was injected into one group of the mice as a control. After allowing an accumulation time of 20 hr, the tumors were imaged using OCT. Representative OCT images (Figure 19) reveal significant increase in contrast intensity in tumors of mice treated with nanoshells and no contrast intensity increase in tumors of mice not receiving nanoshells. Quantification of this intensity increase is shown in Figure 20.

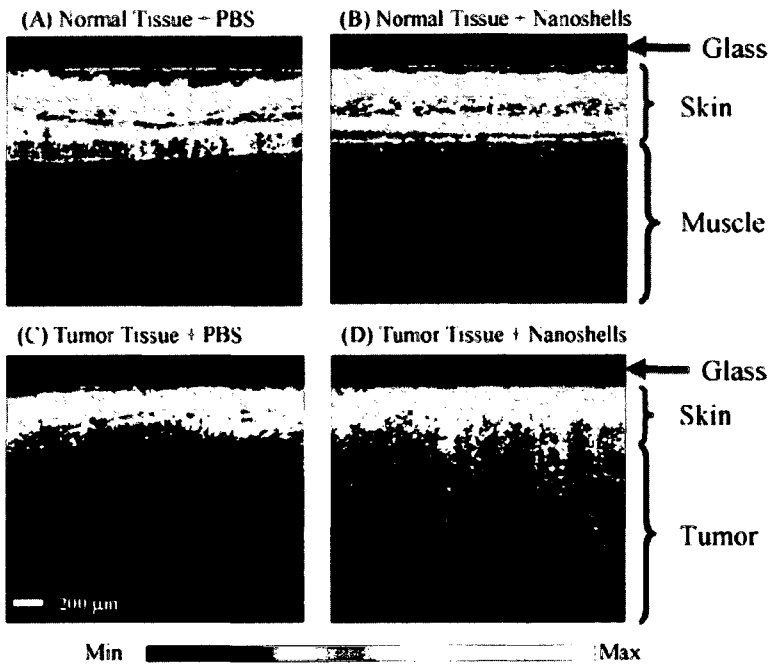

Figure 19 Representative OCT images of skin/muscle areas (A and B) or tumor areas (C and D) of mice injected with PBS (A and C) or nanoshells (B and D). Increase in contrast between normal tissue and tumor tissue is apparent in mice with nanoshells but not those injected with PBS[70].

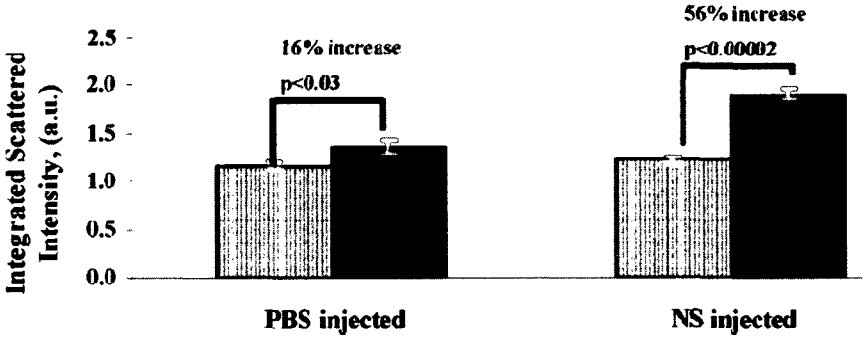

Figure 20 Quantification of OCT image intensity reveals a significant difference in intensity between normal (gray bar) and tumor tissue (black bar) of mice injected with nanoshells and no significant difference between the intensity of tissues in those mice injected with PBS[70].

Following OCT imaging, mice were randomly divided into three groups. These comprised of the treatment group (nanoshells + laser), sham group (PBS + laser), and control group (untreated). The tumors of the treatment and sham groups were irradiated with a NIR laser (808 nm, 4 W/cm^2, 3 min), after which tumor size and animal survival were monitored for the next 7 weeks. Twelve days after treatment, all but 2 tumors in the

treatment group had regressed while tumors of those mice in the sham and control groups continued to grow (Figure 21A). By day 21 after treatment, survival of the treatment group was significantly greater than either the sham or control groups (Figure 21B).

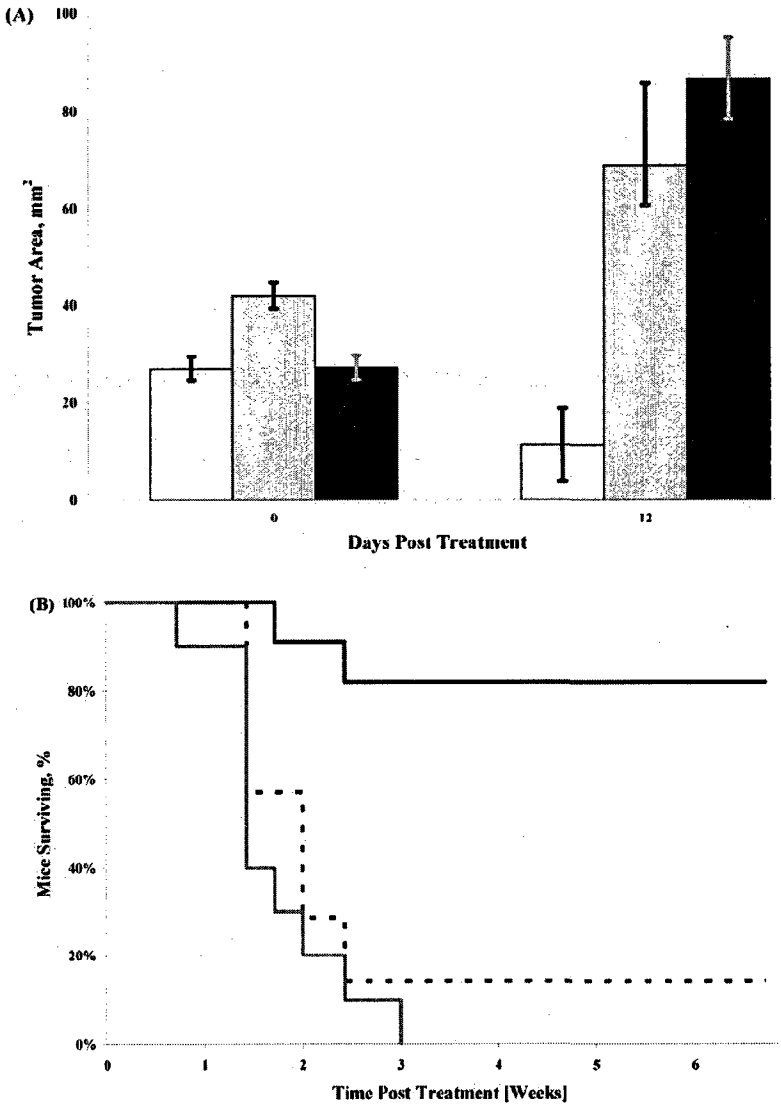

Figure 21 Tumor size and survival following NAPT. **(A)** Tumor size before treatment and 12 days after treatment for treatment group (white bar), sham group (grey bar), and control group (black bar). Tumor size decreased for those mice receiving nanoshells + laser treatment but increased in those receiving PBS + laser and those receiving no treatment. **(B)** Kaplan-Meier survival curve indicates survival of 80% of those mice receiving nanoshells + laser treatment 7 weeks after treatment (black line)[70].

1.6.6 Advantages of Nanoshell Therapy

There are many advantages to using nanoshells in treatment of tumors as opposed to current treatment methods. The peak optical absorption of nanoshells can be tuned to the NIR region and can therefore absorb light and generate heat when irradiated with a NIR laser. Due to the low absorption and high transmittance of light in the NIR range in tissues, irradiation does not cause damage to the skin or surrounding tissue. This therefore provides a safe non-invasive method of photothermal ablation of tumors.

Current chemotherapeutic therapy involves systemically administering anti-proliferative drugs, often destroying healthy cells. The facile conjugation of biomolecules to the nanoshell surface enables tumor-specific targeting of the nanoshells. The nanoshells can be targeted to molecules on the surface of the tumor cells[63] or to receptors on the endothelium, specifically targeting the tumor vasculature[64]. This tumor-specific targeting enables more rapid accumulation of the nanoshells within the tumor[60, 64]. Laser irradiation of the tumor containing targeted nanoshells results in localized tumor cell death.

The combined scattering and absorbing properties of nanoshells enables them to be used in combined imaging and therapy applications[63, 68, 69] Subsequently, nanoshells can be used simultaneously as an imaging contrast agent and therapeutic agent. Following injection of the nanoshells, tumors can be localized through scatter-based imaging methods and then immediately irradiated for tumor photothermal ablation. This is potentially advantageous to the patient due to more rapid therapy upon tumor localization.

1.7 Project Summary

In order to increase specificity of the nanoshell therapy to the tumor area and to limit unwanted heating in surrounding tissues, the nanoshells were cross-linked with a peptide degradable by the MMPs in the tumor interstitium. These nanoshells experience a broadening and red-shifting of the peak, resulting in the inability to generate as much heat when irradiated at their initial peak wavelength. Once the linker is degraded by the MMPs in the tumor, the peak properties return, leading to the ability to generate heat and cause tumor cell death. Those nanoshell aggregates that remain outside the tumor area and are therefore not exposed to higher levels of MMPs will remain aggregated and unable to generate high amounts of heat.

Due to the dampened peak optical properties, the nanoshell aggregates will not absorb as much energy and therefore not experience as extensive heating as dispersed nanoshells. The peak optical properties should be regained by degradation of the linker by the matrix metalloproteases (MMPs) activated in the tumor.

The degradable peptide selected was GGLGPAGGK, due to its collagenase-specificity. A 2300 Da poly(ethylene) glycol (PEG) chains was added to each end of the peptide in order to provide the enzyme enough space to fit between the nanoshells in order to cleave the peptide.

Chapter 2: Materials and Methods

2.1 Fabrication of Gold-Silica Nanoshells

Nanoparticles consisting of a dielectric silica core and a gold shell were made according to the four-step process outlined below[53].

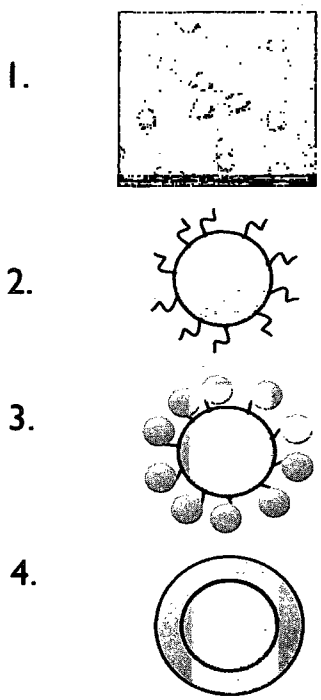

Figure 22. Four-step synthesis of silica-gold nanoshell fabrication

2.1.1 Silica Particle Formation

Solid silica nanoparticles were formed according to the Stöber method[71]. For particle sizes in the range of 80 – 140 nm, the following procedure was followed. Concentrated ammonium hydroxide at a volume of 2.5-3.1 mL, (NH_4OH, Aldrich, 28%) was added to 45 mL of ethanol (EtOH). The core size correlates with the amount of NH_4OH added. While stirr tetraethylorthosilicate (TEOS, Aldrich 99.999%) was added after which the mixture rapidly stirred for 1 min. The mixture was allowed to stir slowly for a period of at least 8 hr while the condensation reaction of the silica progressed. The silica nanoparticles were centrifuged twice (1900 x g, 30 min.) each time being re-suspended in fresh 100% ethanol. The sizes of the silica nanoparticles were measured using scanning electron microscopy (SEM; Quanta FIE 400). Batches of particles with a polydispersity less than 10% were used in the subsequent steps.

2.1.2 Functionalization of Silica Particles

To promote binding of small gold colloid to the silica particle, the surface was

terminated with amine groups[53, 72]. 3-aminopropyltriethoxysilane (APTES, Aldrich, 99%) at a volume of 100-200 μL was added to each batch of cores and allowed to react for at least 8 hr. The cores were then boiled at constant EtOH volume for 2 hr to promote covalent bonding of the silane groups to the surface of the silica particles. The cores were then again centrifuged twice (1900 x g, 30 min.) and re-suspended in fresh EtOH.

2.1.3 Gold Colloid Formation and Seed Growth

Gold colloid was prepared as described by Duff[73]. A stock solution of tetrakis(hydroxymethyl)phosphonium chloride (THPC, Aldrich) was made by the addition of 400 μl of THPC to 33 ml of deionized (DI) water. While stirring rapidly, 4 ml of the THPC stock and 1.2 ml of 1 M NaOH (Aldrich) were added to 180 ml of DI water chilled to 4°C. After allowing the solution to stir for 5 min, 6.75 ml of 1% chloroauric acid ($HAuCl_4$, Aldrich, 99.999%) was added, resulting in a light reddish-brown suspension of colloid. The colloid was aged 2-3 days at room temperature.

The "seed particle," a silica nanoparticle with gold colloid bound to the surface served as the precursor to the gold-silica nanoshell[53, 72]. To make seed particles, a 180 ml volume of colloid was mixed with 1 ml of functionalized cores at 4 wt%. 9 mL of 1 M NaCl was also added to the mixture. This was allowed to react up to 3 days at 4°C. The resulting seed particles were washed with DI water through centrifugation (1300 x g,15 min, performed twice) with ultrasonic probe resuspension. Finally, seed particles were diluted with DI water to have an extinction of 0.1 A.U. at a wavelength of 530 nm.

2.1.4 Shell Formation

The final step in formation of the nanoshell is the formation of the gold shell on the surface of the silica core. 3 ml of 1% $HAuCl_4$ was added to 200 ml of 1.8 mM potassium carbonate (K_2CO_3, Aldrich) and allowed to age a minimum of 12 hr. The necessary volume ratio of seed suspension to potassium carbonate solution to produce nanoshells with the desired extinction characteristics was determined by examining the UV-Vis spectra of varying ratios at a total volume of 1 mL. Once the appropriate ratio was determined, the appropriate volume ratio is scaled up to produce larger amounts of nanoshells. Seed was mixed with the $HAuCl_4/K_2CO_3$ solution and while rapidly mixing, formaldehyde at a volume of 10 μl per 1 ml $HAuCl_4/K_2CO_3$ was added, reducing the gold and resulting in a contiguous gold shell over the surface of the silica particle. The characteristics of the nanoshell were determined by spectral extinction profile using a UV-Vis spectrophotometer (Cary Bio 50) in the range of 400 – 1100 nm. After analysis the nanoshells were washed with a 1.8 mM potassium carbonate solution then centrifuged (700 x g, 20 min, performed twice) . The final nanoshells were re-suspended in DI water.

2.2 Peptide Synthesis

The collagenase-sensitive peptide, GGLGPAGGK, was made using Fmoc solid phase peptide synthesis. This method involves the use of a polystyrene bead resin on which the amino acids are added one by one. The schematic of solid phase peptide synthesis is shown in Figure 23. After addition of the first amino acid to the polystyrene bead, the Fmoc protecting group is removed. The C terminus of the next amino acid is activated after which it is coupled to the amino acid on the resin. This process is

completed until the desired amino acid sequence is achieved. The last Fmoc group and any other side chain protecting groups are then removed followed by cleavage of the peptide from the resin.

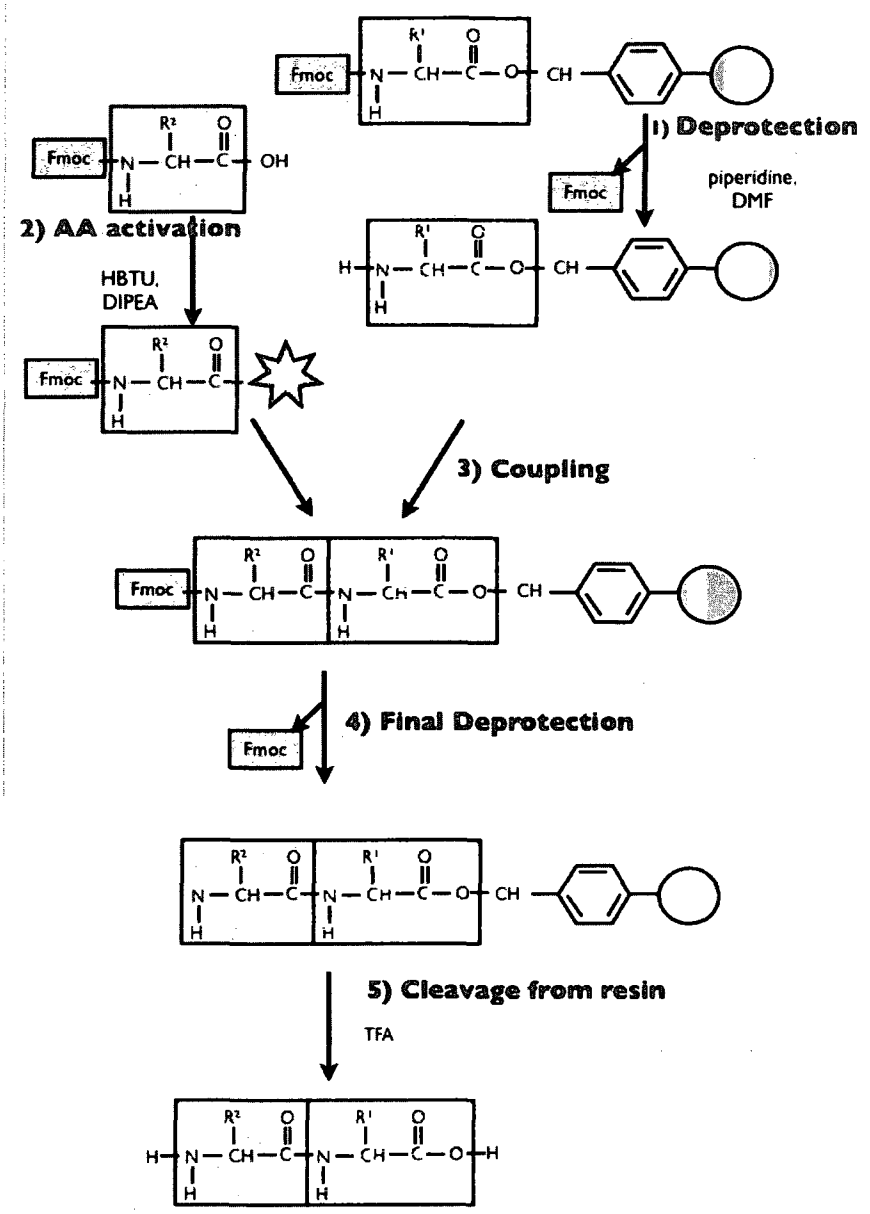

Figure 23. In solid phase peptide synthesis, amino acids are added in chain-like fashion onto a solid bead resin. Amino acid coupling involves the following steps: (1) removal of the protecting group from amino acid A, (2) activation of the C-terminus of amino acid B, and (3) coupling of the amino acids A and B. These steps are repeated until the peptide chain reaches the desired length after which the final protecting group is removed (4) and then the peptide chain is cleaved from the resin (Adapted from [74]).

The peptide was synthesized using Fmoc solid-phase synthesis on an automated peptide synthesizer (Aapptec). The following solutions of organic solvents were made up for the synthesis process: 25% piperidine (Sigma) in dimethylformamide (DMF, Sigma), 2M diisopropylethylamine (DIPEA, Sigma) in 1:1 DMF:dichloromethane (DCM, Applied Biosystems), and 0.5M HBTU (o-Benzotriazol-1-yl-N,N,N',N'-tetramethyluronium hexafluorophosphate, Novabiochem) in DMF. 0.2273 g Fmoc-Lys(Boc)-Wang resin (Novabiochem) was placed in each of the 8 wells on the reaction block. Amino acids were dissolved to 0.5 M in appropriate volumes of 1:1:1 volumetric ratios of N-methyl-pyrrolidinone (NMP, Applied Biosystems):DCM:DMF. The synthesizer performed the steps of solid-phase peptide synthesis including removal of the Fmoc protecting group, amino acid activation and coupling, and washing. Upon completion of the peptide synthesis, the peptide was cleaved from the polystyrene resin using a cleavage cocktail of 95% trifluoroacetic acid (TFA, Sigma), 2.5% triisopropylsilane (TIPS, Sigma), and 2.5% water. This cocktail reacted with peptide-resin on the reaction block in the synthesizer for 3 hr after which the solution, now containing the solubilized peptide was collected. Upon completion of the cleavage step, the TFA was removed from the peptide via rotary evaporation (Büchi Rotavapor R-200). The remaining solution was added to chilled ethyl ether anhydrous (Fisher Scientific), resulting in precipitation of the peptide. Residual cleavage cocktail was removed from the precipitate via centrifugation (1900 x g, 30 minutes, repeated 5 times). After the final centrifugation step, the supernatant was decanted and the peptide was left to dry overnight. After drying, the peptide was dissolved in water and dialyzed against DI H_2O using a 500 Da molecular weight cut-off

membrane for 8 hr, changing the water every hour. Upon completion of dialysis, the peptide solution was frozen and then lyophilized. The final lyophilized peptide was characterized via MALDI-TOF mass spectrometry (MS Autoflex) and stored under argon at -80°C.

2.3 PEG Conjugation to Peptide

The peptide sequence GGLGPAGGK was conjugated to a bi-functional PEG molecule, orthopyridyl sulfide–PEG–n–hydroxysuccinimide (OPSS–PEG–SPA, Nektar, MW 2000) by reacting a 2.4 molar excess of PEG to peptide in sodium bicarbonate buffer. This allowed primary amines on both ends of the peptide, both on the amino-terminus and the lysine side-chain, to react with the PEG forming peptide bonds via cleavage of the SPA group (Figure 24).

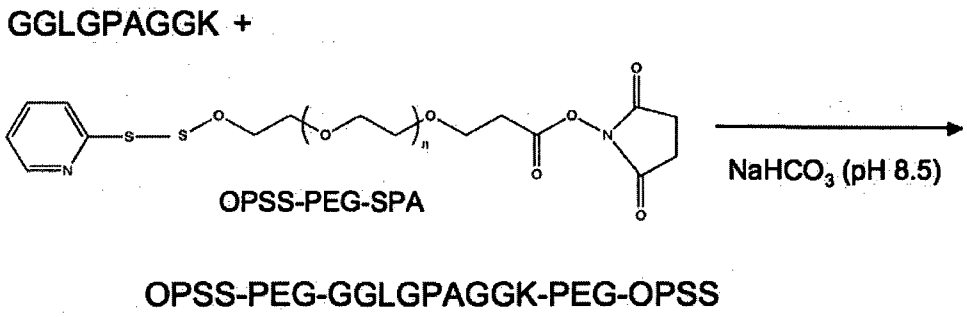

Figure 24. Reaction scheme of PEG-peptide conjugation. The PEG molecule binds to the free amine on each end of the peptide chain via cleavage of the SPA group.

After reacting overnight on a rocker at 4°C, the PEG-peptide-PEG was dialyzed overnight against a membrane of MWCO 3500 Da, lyophilized, and stored frozen in powder form. The PEG-peptide-PEG conjugation was characterized through gel permeation chromatography in order to determine the presence of pure PEG-LGPA-PEG

with no PEG-LGPA or un-reacted OPSS-PEG-SPA (PL-ELS 1000, Polymer Laboratories).

2.4 PEGylation of Nanoshells

In order to prevent nonspecific protein adsorption to the gold surface, the nanoshells were functionalized with PEG-thiol (PEG-SH, Laysan, 5000 Da), the amount of which to be added was determined using the stability test, described below. The thiol group on the end of the PEG chain strongly binds to the gold layer forming a monolayer on the nanoshell surface. Following addition of PEG-SH, the nanoshell suspension was vortexed to ensure proper mixing and then was allowed to react on a rocker at 4°C for 12 hours.

2.5 Nanoshell Stability Test

A stability test was performed in order to determine the minimum amount of PEG-SH necessary for complete coverage of the nanoshells surface. After washing, nanoshells were diluted to a concentration of 4.5×10^9 NS/ml and aliquoted into UV-Vis cuvettes at a 1 ml volume. 4 μl of PEG-SH at concentrations of 0, 0.5, 1.0, 1.5 mM was added to nanoshell cuvettes after which the cuvettes were vortexed and incubated at 4°C overnight. 100 μl of a 1 mM sodium chloride (NaCl) solution was added to each cuvette of nanoshells and the change in the UV-Vis spectrum was recorded every 10 minutes over a period of 2 hours. Those nanoshells that did not have sufficient surface coverage of the PEG-SH aggregated and fell out of solution upon addition of salt to the suspension while those that had full coverage remained suspended. The lowest volume of PEG-SH added to the nanoshells among those that remained suspended upon addition of salt was

considered the lowest amount necessary to provide sufficient surface coverage and stabilize the nanoshells.

2.6 Enzyme-Induced Nanoshell Aggregation Test

The addition of an enzyme to an aqueous suspension of gold nanoparticles, as is necessary to degrade the peptide linker, can result in aggregation of the nanoparticles. Therefore, highest enzyme concentration at which the nanoparticles remain disperse in the suspension must be determined. Silica-gold nanoshells were diluted to a concentration of $4x10^9$ particles/ml. Proteinase K (Invitrogen) was added to the nanoshells resulting in final enzyme concentrations of 0.0025, 0.005, and 0.01 mg/ml. The UV-vis spectrum of each nanoshells suspension was recorded every 10 minutes for 2 hours after addition of the enzyme. Nanoshell aggregation was characterized by a decrease in the peak extinction.

2.7 Heat Measurements of PEG-dithiol-Crosslinked Nanoshells

Nanoshells were made as described above and diluted to a concentration of $4x10^9$ NS/ml. 0.5 μl of 0.1 mM PEG dithiol (SH-PEG-SH, Nektar) was added to 1 mL of the nanoshell suspension and allowed to react overnight. UV-Vis scans were taken every 24 hr and the peak absorbance value was recorded. Each cuvette of nanoshells and PEG dithiol was irradiated with a 808 nm laser at 3 watts for 5 minutes. The temperature of the nanoshell suspension was measured with a thermocouple placed outside the laser beam (Omegaette HH500). The final change in temperature over 5 min was determined and averaged.

2.8 Crosslinking Nanoshells with a Degradable Linker

PEG-LGPA-PEG was mixed with PEG-SH at a final concentration of that which

was determined to be the lowest concentration necessary to stabilize the nanoshells. Nanoshells were concentrated to $4x10^9$ NS/ml and then aliquoted into UV-Vis cuvettes at a volume of 1 ml. 4 μl of the PEG-LGPA-PEG mixtures were added to the appropriate cuvette, immediately after which the nanoshell suspensions were vortexed for 1 second. As a control, the same experiment was run in parallel with PEG-dithiol (SH-PEG-SH, 3400 Da, Laysan Bio Inc.) in place of the PEG-LGPA-PEG. The nanoshells/linker mixtures were allowed to react on the benchtop. The UV-Vis spectrum was recorded 1 hr and 2 hrs following addition of the PEG-LGPA-PEG/PEG-SH or SH-PEG-SH/PEG-SH mixture. A decrease in the peak extinction indicated cross-linking of the nanoshells.

2.9 Degradation of Peptide Linker

Two hours after addition of the PEG-LGPA-PEG/PEG-SH or SH-PEG-SH/PEG-SH mixture, 1.26 μl of 2 mg/ml collagenase (Type XI, Sigma-Aldrich) was added to each cuvette for a final concentration of 0.0025 mg/ml collagenase. The UV-Vis spectrum of each sample was recorded 3 hours following addition of the collagenase.

Chapter 3: Results

3.1 Heating Test

Following addition of 0.5 μl 0.1 mM PEG dithiol to the nanoshell suspension, the peak extinction of the nanoshells decreased overtime as shown in Figure 25. Those nanoshells to which no PEG dithiol was added remained disperse and there was no change in peak extinction over time.

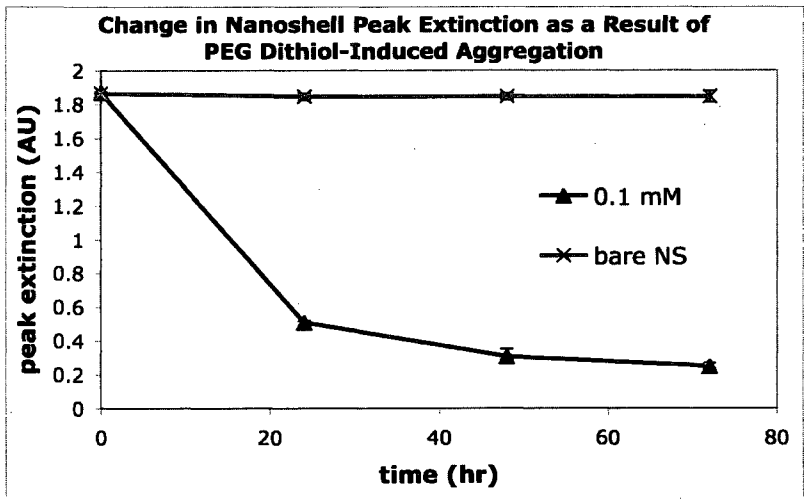

Figure 25 The aggregation of nanoshells resulting from introduction of SH-PEG-SH into the suspension is dependent on the amount of PEG dithiol. Nanoshell aggregation occurred when PEG dithiol at a concentration of 0.1 mM is added but not 1 or 10 mM.

Temperatures of the nanoshell suspensions were recorded with a thermocouple. Those nanoshells cross-linked with PEG-dithiol as indicated by a lower peak extinction had a lower change in temperature ($\Delta T=22°C$) after 5 minutes of heating, than bare nanoshells ($\Delta T=67°C$), as shown in Figure 26.

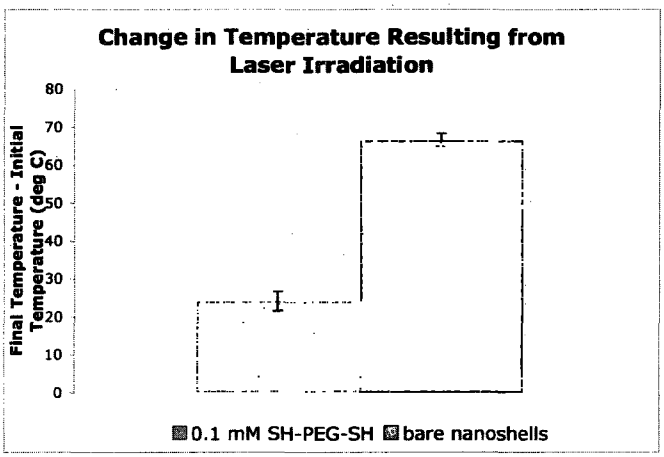

Figure 26 Temperature readings of nanoshell suspensions revealed a lower change in heating in those with aggregated nanoshells than those with disperse nanoshells.

3.2 Enzyme-Induced Nanoshell Aggregation Test

Varying amounts of proteinase K were added to nanoshells in order to determine the highest concentration at which nanoshell protein-induced aggregation would not occur. After 2 hours, the nanoshells remained disperse with a final enzyme concentration of 0.0025 mg/ml and 0 mg/ml (control) but aggregated as a result of the other enzyme concentrations (0.01 mg/ml, 0.005 mg/ml).

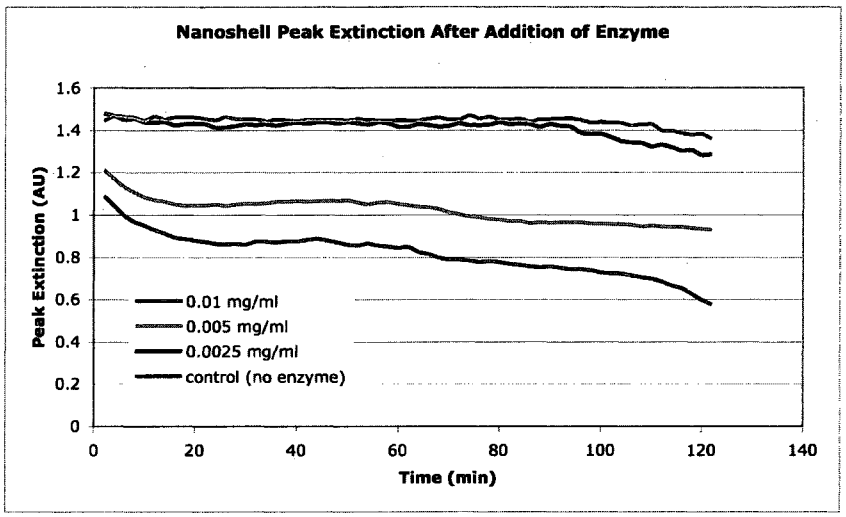

Figure 27 Proteinase K added to a nanoshell suspension at final concentrations of both 0.01 and 0.005 mg/ml induced nanoshell aggregation. A final enzyme concentration of 0.0025 mg/ml allowed the nanoshells to remain suspended.

This data suggests that after the nanoshells are cross-linked with a proteolytically degradable peptide, a maximum of 0.0025 mg/ml enzyme can be added to the nanoshell suspension in order to degrade the peptide and allow the nanoshells to remain suspended.

3.3 Nanoshell Stability Test

This test was performed in order to determine the amount of PEG-SH needed to sufficiently cover the nanoshell surface. Two hours after adding NaCl, the peak absorbance of the nanoshells with 4 μl 1.5 mM PEG-SH had decreased by 6.8%, 1.0 mM by 7/9%, 0.5 mM by 10% and 0 mM by 99% (Figure 28).

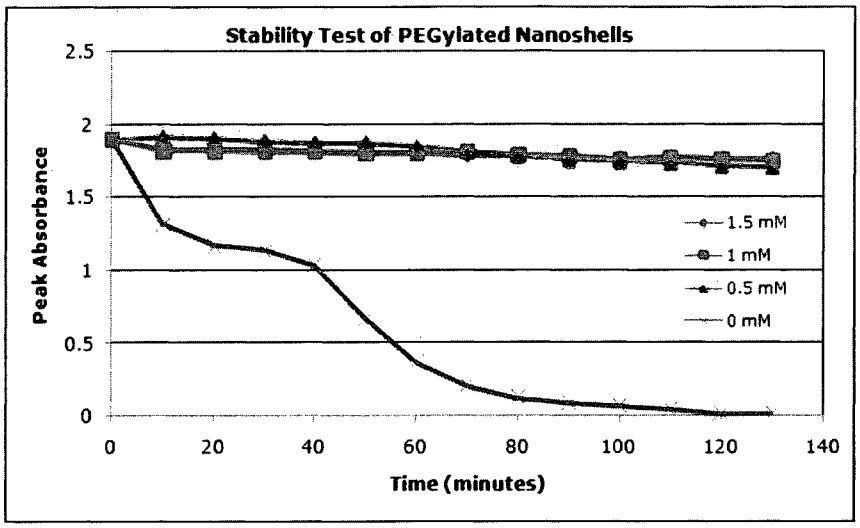

Figure 28. Stability test of PEGylated nanoshells. Nanoshells to which 4 μl of 1.5, 1, and 0.5 mM PEG-SH were added remained stable in the presence of NaCl.

This test suggests that 4 μl 0.5 mM PEG-SH added to nanoshells at a concentration of 4.5 x 10^9 NS/ml is sufficient to cover the surface of the gold nanoshell. This value was used in the subsequent study.

3.4 Crosslinking Nanoshells

0.5 mM SH-PEG-SH/PEG-SH and PEG-LGPA-PEG/PEG-SH mixtures of varying mole fractions were added to 1 mL volumes of nanoshells at a concentration of 4.5 x 10^9 NS/ml. The UV-Vis spectra taken 3 hours after addition of SH-PEG-SH/PEG-SH mixtures revealed a trend toward a greater decrease in peak absorbance with an increase of SH-PEG-SH mole fraction (Figure 29) The change in peak absorbance (initial absorbance – final absorbance) between mole fractions appears to increase exponentially.

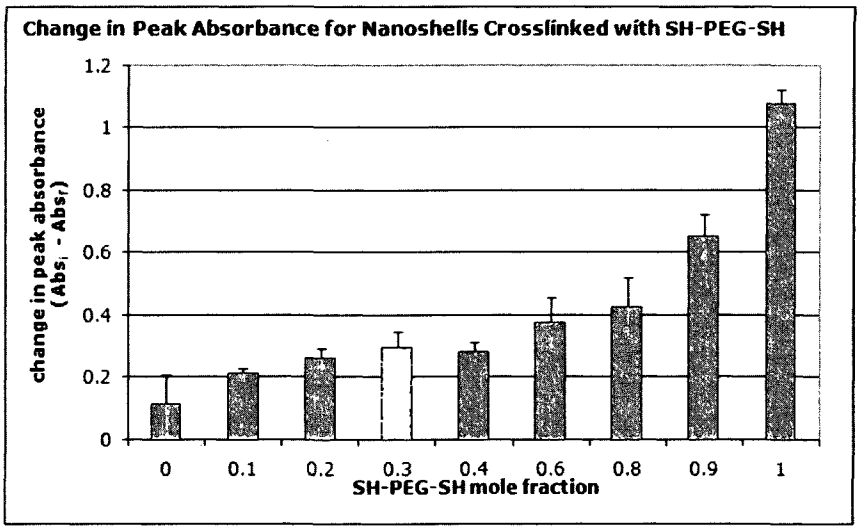

Figure 29. Change in peak absorbance (initial peak absorbance – final peak absorbance) as a result of varying SH-PEG-SH mole fractions mixed with PEG-SH. The decrease in peak is greater with an increase in dithiol mole fraction.

The UV-Vis spectra taken 3 hours after addition of PEG-LGPA-PEG/PEG-SH mixtures revealed a trend toward a greater decrease in peak absorbance among the middle PEG-LGPA-PEG mole fractions, 0.4 being the highest

Figure 30).

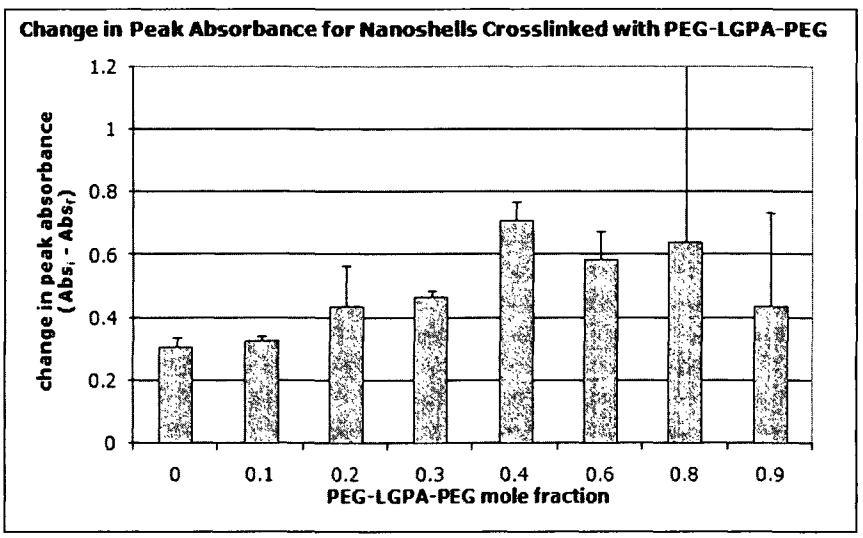

Figure 30. Change in peak absorbance as a result of varying PEG-LGPA-PEG mole fractions mixed with PEG-SH. The decrease in peak absorbance is greater for the middle PEG-LGPA-PEG mole fractions.

3.5 Enzymatic Degradation of Peptide Linker

After cross-linking the nanoshells, 1.26 μl 2 mg/ml collagenase (0.0025 mg/ml final concentration) was added to those nanoshells that experienced the greatest decrease in peak absorbance (1 SH-PEG-SH mole fraction; 0.4 PEG-LGPA-PEG mole fractions) and the resulting peak absorbance was measured after 3 hours. Those nanoshells that had been cross-linked with SH-PEG-SH did not experience an increase in peak absorbance following collagenase addition, while those crosslinked with PEG-LGPA-PEG did experience an increase in peak absorbance (Figure 31).

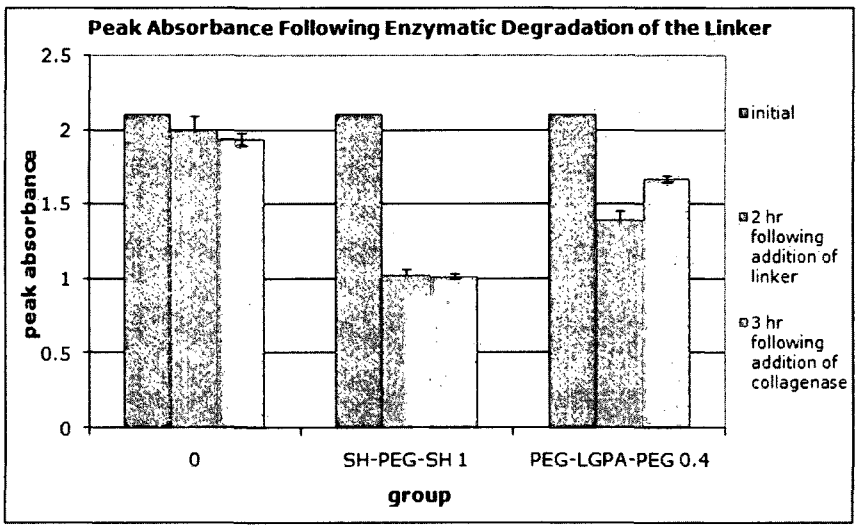

Figure 31. Peak absorbance before and after the addition of linker and after addition of collagenase. The peak increased for the nanoshells crosslinked with PEG-LGPA-PEG, but remained unchanged for the nanoshells crosslinked with SH-PEG-SH.

Chapter 4: Discussion

These studies have shown nanoshells are able to be crosslinked with a dithiol molecule, resulting in a red-shifting and broadening of the UV-Vis spectrum. Crosslinked nanoshells were shown to experience a lower temperature change when irradiated with a near-infrared laser than dispersed nanoshells, as predicted by the presence of a lower peak absorbance value. This study provides a proof-of-principle demonstrating the difference in temperature change is large enough to cause tissue damage through the disperse nanoshells while not causing tissue damage through the crosslinked nanoshells. While the final temperature change of the crosslinked nanoshells in this study (22°C) is above the 15°C threshold for irreversible tissue damage[75], the difference between the final temperatures is enough so that if the laser power were reduced in order to lower the temperature change of the crosslinked nanoshells, the disperse nanoshells would still experience a temperature change high enough to cause irreversible tissue damage.

The results from the crosslinking study suggest that the molar ratios of dithiol molecule to PEG-SH have an effect on nanoshell cross-linking. These studies were done by adding 4 μl of a 0.5 mM thiolated molecule mixture to 1 ml nanoshells. For this thiolated molecule concentration, when the nanoshells were crosslinked with SH-PEG-SH, the change in the peak absorbance seems to increase exponentially as the mole fraction increases up to 1. The data shows that when 4 μl of a 0.5 mM PEG-LGPA-PEG/PEG-SH mixture is added to 1 ml nanoshells, the molar concentration of PEG-LGPA-PEG and PEG-SH should be equal (0.4 - 0.6 PEG-LGPA-PEG mole fraction) in order to obtain the greatest decrease in peak absorbance. These results suggests that the

PEG-SH sterically aids the dithiol molecule (PEG-LGPA-PEG or SH-PEG-SH) in remaining upright on the nanoshell surface and exposing its other end to other nanoshells. Because of the length of the PEG-LGPA-PEG and SH-PEG-SH linker, a low presence of PEG-SH may allow the linker molecules to bend back on themselves, binding both ends to one nanoshell. The difference in dithiol molecule/PEG-SH ratios necessary to achieve the greatest decrease in peak may be due to the difference in length between PEG-LGPA-PEG (5000 Da) and SH-PEG-SH (3400 Da).

After crosslinking the nanoshells with SH-PEG-SH and PEG-LGPA-PEG, collagenase was added and the effects were observed. Three hours following addition of the enzyme to nanoshells crosslinked with PEG-LGPA-PEG, the peak made a significant increase, although not to the original peak absorbance value. Addition of enzyme to the nanoshells crosslinked with SH-PEG-SH made no difference in the peak absorbance. This increase in peak for PEG-LGPA-PEG crosslinked nanoshells but not for the SH-PEG-SH crosslinked nanoshells indicates a degradation of the peptide linker leading to a dispersion of nanoshells crosslinked with PEG-LGPA-PEG.

Chapter 5: Conclusion

This work has shown the ability of silica-gold nanoshells to be crosslinked with a dithiol molecule resulting in a decrease in peak absorbance. This decrease in peak absorbance was shown to correlate with a decrease in ability to generate heat upon laser irradiation, leading to a lower temperature change compared to disperse nanoshells.

Crosslinking nanoshells with the degradable peptide-containing linker OPSS-PEG-GGLGPAGGK-PEG-OPSS was shown to occur to the greatest extent when equal molar amounts of PEG-SH and the linker were present. The degradation of this linker was demonstrated by an increase in peak absorbance of the nanoshells following the addition of collagenase while those nanoshells crosslinked with a non-degradable linker did not experience an increase in peak absorbance.

These studies have laid the groundwork for further development of protease-activated nanoshell therapy. Further studies should be done to control aggregate size to one small enough to be able to extravasate out of the tumor vasculature. *In vitro* studies should be done with a highly metastatic cell line, such as HT-1080 in order to demonstrate successful nanoshell therapy when nanoshells crosslinked with a degradable linker are placed in the presence of secreted MMPs.

References

1. *American Cancer Society, Cancer Facts & Figures 2007.* 2007 [cited 2007; Available from: http://www.cancer.org.

2. *United States Cancer Statistics: 2003 Incicence and Mortality*, U.S.C.S.W. Group, Editor. 2006, U.S. Department of Health and Human Services, Centers for Disease Control and Prevention: Atlanta.

3. McKinnell, R.G., et al., *The Biological Basis of Cancer.* 1998, New York: Cambridge University Press. 378.
4. Hanahan, D. and R.A. Weinberg, *The Hallmarks of Cancer.* Cell, 2000. **100**: p. 57-70.

5. Carmeliet, P. and R.K. Jain, *Angiogenesis in cancer and other diseases.* Nature 2000. **407**(6801): p. 249-257.

6. Jain, R.K., *Normalization of tumor vasculature: An emerging concept in antiangiogenic therapy.* Science, 2005. **307** : p. 58-62.

7. Helminger, G., et al., *Interstitial pH and pO2 gradients in solid tumors in vivo: high-resolution measurements reveal a lack of correlation.* Nature Medicine, 1997. **3**: p. 177-182.

8. Hashizume, H., et al., *Openings between defective endothelial cells explain tumor vessel leakiness.* American Journal of Pathology, 2000. **156**(4): p. 1363-1380.

9. McDonald, D.M. and A.J. Foss, *Endothelial cells of tumor vessles: abmornal but not absent.* Cancer Metastasis Reviews, 2000. **19**: p. 109-120.

10. McDonald, D.M. and P. Baluk, *Significance of Blood Vessel Leakiness in Cancer.* Cancer Research, 2002. **62**: p. 5381-5385.

11. Hobbs, S.K., et al., *Regulation of transport pathways in tumor vessels: Role of tumor type and microenvironment.* Proceedings of the National Academy of Sciences of the United States of America, 1998. **95**(8): p. 4607-4612.

12. Leu, A.J., et al., *Absence of functional lymphatics within a murine sarcoma: a molecular and functional evaluation.* Cancer Research, 2000. **60**: p. 4324-4327.

13. Maeda, H., *The enhanced permeability and retention (EPR) effect in tumor vasculature: the key role of tumor-selective macromolecular drug targeting.* Advances in Enzyme Regulation, 2001. **41**: p. 189-207.

14. Duffy, M.J., et al., *Metalloproteinases: role in breast carcinogenesis, invasion and metastasis.* Breast Cancer Research, 2000. **2**: p. 252-257.

15. Chambers, A.F. and L.M. Matrisian, *Changing views of the role of matrix metalloproteinases in metastasis.* Journal of the National Cancer Institute, 1997. **89**: p. 1260-1270.

16. Nagase, H., R. Visse, and G. Murphy, *Structure and function of matrix metalloproteinases and TIMPs.* Cardiovascular Research, 2006. **69**: p. 562-573.

17. *Matrix Metalloproteinases.* 2007 [cited 2007; Available from: www.emdbiosciences.com/html/cbc/matrix_metalloproteinases.

18. Nelson, A.R., et al., *Matrix Metalloproteinases: Biologic Activity and Clinical Implications.* Journal of Clinical Oncology, 2000. **18**: p. 1135-1149.

19. Polette, M. and P. Birembaut, *Membrane-type metalloproteinases in tumor invasion.* The International Journal of Biochemistry & Cell Biology, 1998. **30**: p. 1195-1202.

20. Liotta, L.A., et al., *Metastatic potential correlates with enzymatic degradation of basement membrane collagen.* Nature, 1980. **284**(1): p. 67-68.

21. Nakajima, M., et al., *Degradation of basement membrane type IV collagen and lung subendothelial matrix by rat mammary adenocarcinoma cell clones of differing metastatic potentials.* Cancer Research, 1987. **47**: p. 4869-4876.

22. Sato, H., et al., *A matrix metalloproteinase expressed on the surface of invasive tumour cells.* Nature, 1994. **370**: p. 61-65.

23. Sounni, N.E., et al., *MT1-MMP expression promotes tumor growth and angiogenesis through an up-regulation of vascular endothelial growth factor expression.* The FASEB Journal , 2002. **16**: p. 555-564.

24. Patel, B.P., et al., *Clinical significance of MMP-2 and MMP-9 in patients with oral cancer.* Head & Neck, 2007. **29**(6): p. 564-572.

25. Shim, K.N., et al., *Clinical significance of tissue levels of matrix metalloproteinases and tissue inhibitors of metalloproteinases in gastric cancer.* Journal of Gastroenterology, 2007. **42**(2): p. 120-128.

26. Bonomi, P., *Matrix metalloproteinases and matrix metalloproteinase inhibitors in lung cancer.* Seminars in Oncology, 2002. **29**(1 Suppl. 4): p. 78-86.

27. Boag, A.H. and I.D. Young, *Increased expression of the 72-kD type IV collagenase in prostatic adenocarcinoma. Demonstration by immunohistochemistry and in situ hybridization.* American Journal of Pathology, 1994. **144**: p. 585-591.

28. Afzal, S., et al., *MT1-MMP and MMP-2 mRNA expression in human ovarian tumors: possible implications for the role of desmoplastic fibroblasts.* Human Pathology, 1998. **29**: p. 155-165.

29. Sakata, K., et al., *Expression of matrix metalloproteinases (MMP-2, MMP-9, MT1-MMP) and their inhibitors (TIMP-1, TIMP-2) in common epithelial tumors of the ovary.* International Journal of Oncology, 2000. **17**: p. 673-681.

30. Davies, B., J. Waxman, and H. Wasan, *Levels of matrix metalloproteases in bladder cancer correlate with tumor grade and invasion.* Cancer Research, 1993. **53**(22): p. 5365-5369.

31. Rha, S.Y., et al., *Different expression patterns of MMP-2 and MMP-9 in breast cancer.* Oncology Reports, 1998. **5**(4): p. 875-879.

32. Jinga, D.C., et al., *MMP-9 and MMP-2 gelatinases and TIMP-1 and TIMP-2 inhibitors in breast cancer: correlations with prognostic factors.* Journal of Cellular and Molecular Medicine, 2006. **10**(2): p. 499-510.

33. Ii, M., et al., *Role of matrix metalloproteinase-7 (matrilysin) in human cancer invasion, apoptosis, growth and angiogenesis.* Experimental Biology and Medicine, 2006. **231**: p. 20-27.

34. Lynch, C.C. and L.M. Matrisian, *Matrix metalloproteinases in tumor-host cell communication.* Differentiation , 2002. **70**: p. 561-573.

35. Wang, F.Q., et al., *Matrilysin (MMP-7) promotes invasion of ovarian cancer cells by activation of progelatinase.* International Journal of Cancer, 2005. **114**: p. 19-31.

36. *National Cancer Institute. Radiation Therapy for Cancer.* 2004 [cited 2007; Available from: www.cancer.gov.

37. Mangar, S.A., et al., *Technological advances in radiotherapy for the treatment of localised prostate cancer.* European Journal of Cancer, 2005. **41**(6): p. 908-921.

38. Tobias, J.S., et al., *Breast-conserving surgery with intra-operative radiotherapy.* Clinical Oncology, 2006. **18**: p. 220-228.

39. Chronowski, G.M. and T.A. Buchholz, *Accelerated partial breast irradiation.* Current Problems in Cancer, 2007. **31**(1): p. 7-25.

40. Moore-Higgs, G.J., *Radiation options for early stage breast cancer.* Seminaras in Oncology Nursing, 2006. **22**(4): p. 233-241.

41. Middleton, M.R. and G.P. Margison, *Improvement of chemotherapy efficacy by inactivation of DNA-repair pathway.* Lancet Oncology, 2003. **4**: p. 37-44.

42. Valentine, A.M., et al., *Chemotherapeutic agents for colorectal cancer with a defective mismatch repair system: The state of the art.* Cancer Treatment Reviews, 2006. **32**: p. 607-618.

43. Trachsel, E. and D. Neri, *Antibodies for angiogenesis inhibition, vascular targeting, and endothelial cell transcytosis.* Advanced Drug Delivery Reviews, 2006. **58**: p. 735-754.

44. Dougherty, T.J., et al., *Photodynamic therapy.* Journal of the National Cancer Institute, 1998. **90**(12): p. 889-905.

45. Yezhelyev, M.V., et al., *Emerging use of nanoparticles in diagnosis and treatment of breast cancer.* Lancet Oncology, 2006. **7**: p. 657-667.

46. Averitt, R.D. and N.J. Halas, *Plasmon resonance shifts of Au-coated Au2S nanoshells: Insight into multicomponent nanoparticle growth.* Physical Review letters, 1997. **78**(22): p. 4217-4220.

47. Gelderblom, H., et al., *Cremophor EL: The drawbacks and advantages of vehicle selection for drug formulation.* European Journal of Cancer, 2001. **37**: p. 1590-1598.

48. Sparreboom, A., C.D. Scripture, and V. Trieu, *Comparative preclinical and clinical pharmacokinetics of a cremophor-free nanoparticle albumin-bound paclitaxel (ABI-007) and paclitaxel formulated in Cremophor (Taxol).* Clinical Cancer Research, 2005. **11**: p. 4136-4143.

49. Svenson, S. and D.A. Tomalia, *Dendrimers in biomedical applications: reflections on the field.* Advanced Drug Delivery Reviews, 2005. **57**: p. 2106-2129.

50. Bianco, A., K. Kostarelos, and M. Prato, *Applications of carbon nanotubes in drug delivery.* Current Opinion in Chemical Biology, 2005. **9**: p. 674-679.

51. Cho, S.-J., et al., *Gold-coated iron nanoparticles: a novel magnetic resonance agent for T1 and T2 weighted imaging.* Nanotechnology, 2006. **17**: p. 640-644.

52. Rabin, O., et al., *An X-ray computed tomography imaging agent based on long-circulating bismuth sulphide nanoparticles.* Nature Materials, 2006. **5**: p. 118-122.

53. Oldenburg, S.J., et al., *Nanoengineering of optical resonances.* Chemical Physics Letters, 1998. **288**: p. 243-247.

54. Gobin, A.M., et al., *Near infrared laser-tissue welding using nanoshells as an exogenous absorber.* Lasers in Surgery and Medicine, 2005. **37**(2): p. 123-129.

55. Hirsch, L.R., et al., *A whole blood immunoassay using gold nanoshells.* Analytical Chemistry, 2003. **75**: p. 2377-2381.

56. Averitt, R.D., S.L. Westcott, and N.J. Halas, *Linear optical properties of gold nanoshells.* Journal of the Optical Society of America. B, Optical physics, 1999. **16**(10): p. 1824-1832.

57. Zhou, H.S., I. Honma, and H. Komiyama, *Controlled synthesis and quantum-size effect in gold-coated nanoparticles.* PHysical Review B, 1994. **50**(16): p. 12052-12057.

58. Draine, B., *The discrete-dipole approximation and its application to interstellar graphite grains.* The Astrophysical Journal, 1988. **333**: p. 848-872.

59. Lazarides, A.A. and G.C. Schatz, *DNA-linked metal nanosphere materials: structural basis for the optical properties.* Journal of Physical Chemistry B, 2000. **104**: p. 460-467.

60. Weissleder, R., *A clearer vision for in vivo imaging.* Nature Biotechnology, 2001. **19**: p. 316-317.

61. O'Neal, D.P., et al., *Photo-thermal tumor ablation in mice using near infrared-absorbing nanoparticles.* Cancer Letters, 2004. **209**: p. 171-176.

62. Hirsch, L.R., et al., *Nanoshell-mediated near-infrared thermal therapy of tumors under magnetic resonance guidance.* Proceedings of the National Academy of Sciences of the United States of America, 2003. **100**(23): p. 13549-13554.

63. Loo, C., et al., *Immunotargeted nanoshells for integrated cancer imaging and therapy.* Nano Letters, 2005. **5**(4): p. 709-711.

64. Lowery, A.R., *Nanoshell-Assisted Cancer Therapy: Targeted Photothermal Tumor Ablation*, in *Bioengineering*. 2007, Rice University: Houston, TX. p. 122.

65. Brown, L.F., et al., *Expression of vascular permeability factor (vascular endothelial growth factor) and its receptors in breast cancer.* Human Pathology, 1995. **26**: p. 86-91.

66. Brown, L.F., et al., *Expression of vascular permeability factor (vascular endothelial growth factor) and its receptors in adenocarcinomas of the gastrointestinal tract.* Cancer Research, 1993. **53**: p. 4727-4735.

67. Easty, D.J., M. Herlyn, and D.C. Bennett, *Abnormal protein tyrosine kinase gene expression during melanoma progression and metastasis.* International Journal of Cancer, 1995. **60**: p. 129-136.

68. Loo, C., et al., *Nanoshell-enabled photonics-based imaging and therapy of cancer.* Technology in Cancer Research & Treatment, 2004. **3**(1): p. 33-40.

69. Loo, C., et al., *Gold nanoshell bioconjugates for molecular imaging in living cells.* Optics Letters, 2005. **30**(9): p. 1012-1014.

70. Gobin, A.M., et al., *Near-infrared resonant nanoshells for combined optical imaging and photothermal cancer therapy.* Nano Letters, In Press.

71. Stober, W., A. Fink, and E. Bohn, *Controlled growth of monodisperse silica spheres in the micron size range.* Journal of Colloid and Interface Science, 1968. **26** : p. 62-69.

72. Westcott, S.L., et al., *Formation and adsoroption of clusters of gold nanoparticles onto functionalized silica nanoparticle surfaces.* Langmuir, 1998. **14**: p. 5396-5401.

73. Duff, D.G., et al., *A new hydrosol of gold clusters. 2. A comparison of some different measurement techniques.* Langmuir, 1993. **9**: p. 2310-2317.

74. Nelson, D.R. and M.M. Cox, *Lehninger Principles of Biochemistry.* 4 ed. 2005, New York, NY: W.H. Freeman and Company.

75. Hirsch, L.R., et al., *Metal nanoshells.* Annals of Biomedical Engineering, 2006. **34**(1): p. 15-22.